INVESTIGATION OF MICROSTRUCTURE OF UTERINE FIBROIDS IN MAGNETIC RESONANCE GUIDED HIGH INTENSITY FOCUSED ULTRASOUND THERAPY

A Dissertation
Presented to
the Faculty of the Physics Department
University of Houston

In Partial Fulfillment
of the Requirements for the Degree
Doctor of Philosophy

By
Feifei Qu

August 2015

INVESTIGATION OF MICROSTRUCTURE OF UTERINE FIBROIDS IN MAGNETIC RESONANCE GUIDED HIGH INTENSITY FOCUSED ULTRASOUND THERAPY

Feifei Qu

APPROVED:

Dr. Pei-Herng Hor, Chariman

Dr. Raja Muthupillai
St Luke's Episcopal Hospital

Dr. Wu-Pei Su

Dr. Chin-Sen Ting

Dr. Shu-Heng Pan

Dr. Donald Kouri

Dean, College of Natural Sciences and Mathematics

ACKNOWLEDGEMENTS

I would like to express my gratitude and appreciation to my advisors, Dr. Pei-Herng Hor and Dr. Raja Muthupillai for their guidance and support throughout this work. My sincerest appreciation goes to Dr. Wu-Pei Su, Dr. Chin-Sen Ting, Dr. Shu-Heng Pan, and Dr. Donald Kouri for helping me in the APE and thesis defense. I would also like to thank Dr. Amol Pednekar and Dr. Ramkumar Krishnamurthy for helping me study the basic MRI physics. And last, I would like to thank Dr. John Fischer, Clauido Arena, Janie Guerra, Debra Dees, and Melissa Andrews for the clinical and MR scanner operation support.

INVESTIGATION OF MICROSTRUCTURE OF UTERINE FIBROIDS IN MAGNETIC RESONANCE GUIDED HIGH INTENSITY FOCUSED ULTRASOUND THERAPY

An Abstract

of a

Dissertation

Presented to

the Faculty of the Department of Physics

University of Houston

In Partial Fulfillment

of the Requirements for the Degree

Doctor of Philosophy

By

Feifei Qu

August 2015

Abstract

Uterine fibroids are the most common benign tumors in women. Uterine fibroids can cause substantial symptoms including heavy menstrual bleeding, pelvic pressure, and discomfort. MR guided high intensity focused ultrasound (MRgHIFU) uses MRI to monitor thermal ablation of uterine fibroids. It is non-invasive and requires a short recovery time. However, MRgHIFU therapy has several challenges: (1) The long pre-imaging time, which reduces the treatment efficiency and can cause significant patient discomfort. (2) Not all the fibroids are treatable by HIFU therapy. Current studies reported the fibroids with higher signal intensity than muscle and myometrium in T_2-weighted image cannot be treated by this method. (3) Evaluation of treatment response requires the use of a MRI contrast based method, which is contra-indicated in patients with dysfunctional kidney.

This dissertation focused on strategies to address the aforementioned challenges in MRgHIFU therapy of uterine fibroids via numerical simulations and *in vivo* animal and human studies. The specific contributions from this dissertation are as follows: (1) The scan time of conventional T_2-weighted turbo spin echo (TSE) sequence used to obtain pre-treatment images for MRgHIFU therapy was halved by modifying the TSE sequence with variable refocusing flip angles as well as the application of orthogonal 90°-180° radio-frequency pulses to restrict imaging field-of-view. (2) An intra-voxel incoherent motion (IVIM) based model is proposed in lieu of the current approaches to

assess tissue microstructure (diffusion and perfusion) to distinguish treatable and non-treatable fibroids. It is found that with T_2-correction, f (blood volume ratio in IVIM) is different for different types of fibroids. (3) Three potential non-contrast based methods to estimate the treatment outcome are proposed. They include the diffusion weighted imaging (DWI), T_2 map, and f map, and preliminary evidence is presented. (4) A DWI method to monitor tissue microstructure changes *during* heating via apparent diffusion coefficient (*ADC*) based surrogates for diffusion and perfusion is also reported.

With further advancement, this work will permit efficient MRgHIFU therapy of uterine fibroids, by reducing pre-treatment imaging time, selection of treatable fibroids based on their microstructure, and monitor treatment outcome during and after MRgHIFU therapy without the need for MRI contrast.

CONTENTS

1. INTRODUCTION

1.1 INTRODUCTION TO UTERINE FIBROIDS

Uterine fibroids are the most common benign tumors in women. Uterine fibroid tissue is composed primarily of smooth muscle cells, and grows in the uterine wall. In a recent study, Baird et al., found that the cumulative incidence of tumors by age 50 was more than 80% in black women and nearly 70% for white women[1]. Although a majority of the women who have uterine fibroids are asymptomatic, these fibroids can cause substantial symptoms, such as heavy menstrual bleeding, pelvic pressure, and discomfort[2]. Farquhar et al. report that among the 600,000 hysterectomies performed annually in the US, nearly 30% are for treating symptomatic uterine leiomyomas[3].

Uterine fibroids are heterogeneous in terms of size, number, location, and cellular content, making it difficult to predict disease progression or treatment outcomes. Some fibroids can be as small as a marble or as large as 40 lbs[2]. Fibroids can vary in number, ranging from a single large fibroid, to multiple fibroids within the uterine cavity. While large fibroids can cause bulk symptoms in women, even small fibroids can cause significant symptoms depending on their location within the uterine cavity.

The classification of uterine fibroids depends on their location; uterine fibroids which are embedded within the wall of uterus are called intramural fibroids. Uterine fibroids which are located in the mucosal layer of the uterus distorting the endometrium or protruding into the endometrial cavity, are named submucosal fibroids, and even a

small submucosal fibroid can cause heavy bleeding. The subserosal fibroids are on the surface of uterus and tend to grow outward (Figure 1-1).

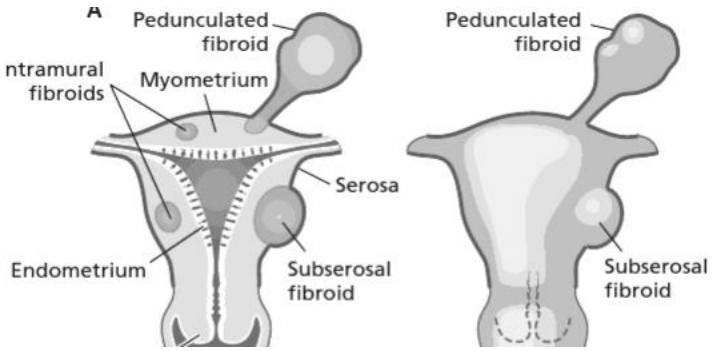

Figure 1-1 *Uterine fibroid classification based on their location within the uterus. Uterine fibroids are classified into 4 types: pedunculated fibroids, subserosal fibroids, intramural fibroids, and submucosal fibroids*[2].

Pedunculated fibroids are those that are on the stalk out of the uterus. The European Society of Hysteroscopy further sub-classifies submucosal fibroids into 3 types based on their location[2]. As it is shown in Figure 1-2, type 0 fibroids are entirely contained in the endometrium. Type I fibroids have at least 50% of their volume in the endometrial cavity, and type II fibroids have at least 50% of their volume in the uterine wall.

With respect to cellular content, although smooth muscle cells are the main constituent of uterine fibroids, the fibroids look different from normal uterine muscle. This is because the amount of extracellular matrix (ECM), which is a collection of proteins and other substances between the cells making them to stick together, is more in uterine fibroids than in the normal uterine muscle (Figure1-3)[4].

The two common symptoms caused by uterine fibroids are heavy menstrual bleeding and pelvic pressure discomfort. The heavy menstrual bleeding is not only

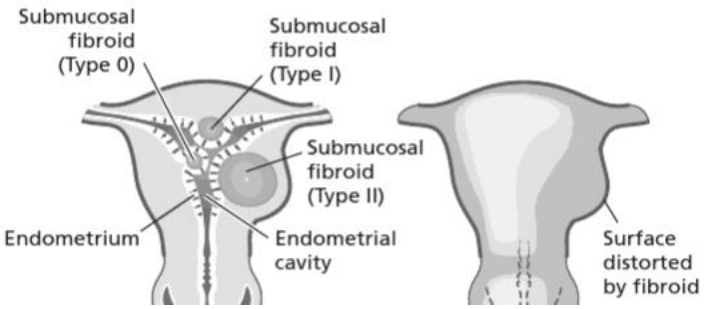

Figure 1-2 *Classification of submucosal fibroids by the European Society of Hysteroscopy*[2].

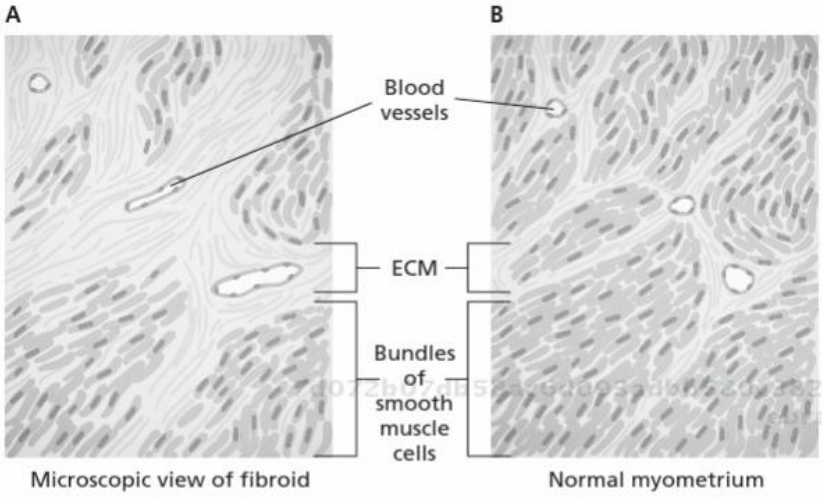

Figure 1-3 *Extracellular matrix (ECM) of normal myometrium and fibroid. A. ECM of uterine fibroids. B. ECM of normal myometrium. The fibroids have more ECM compared with the normal myometrium*[4].

inconvenient but sometimes it can also cause anemia. The pelvic discomfort is typically related to the size of the fibroids and to the pressure on adjacent organs caused by uterus. It can cause increased urinary frequency because the enlarged uterus introduces pressure

on the bladder. It can also cause back pain, abdominal distention, and sciatica which are similar feeling to pregnant.

1.2 CURRENT DIAGNOSIS AND TREATMENT METHODS FOR UTERINE FIBROIDS

Many diagnosis and therapy methods were developed to help women suffering this disease.

The common exposure diagnosis methods not using x-ray exposure include ultrasound[5-7], computed tomography (CT)[8-10] , and magnetic resonance image (MRI) [11-12]. Ultrasound is widely used because it is relatively inexpensive and comfortable for patient. But it is not good at seeing the inside of the uterus or finding small submucosal fibroids. MRI is a radiation-free method. Although it is relatively expensive, it can supply more detailed information for body structure. It can also be applied as a monitoring method during surgical interventions such as MR guided focused ultrasound surgery (MRgHIFU)[13-23]. In procedures such as uterine artery embolization (UAE)[24-32], the treatment is monitored under fluoroscopic x-ray guidance.

The common therapeutic methods for fibroids include hysterectomy[33-35], myomectomy[36-38], UAE, and focused ultrasound surgery (FUS). Hysterectomy is a procedure which removes the whole uterus. It can prevent the recurrence of fibroids, but it is not a preferred choice for women who would like to keep their uterus intact. Myomectomy is the surgical removal of the fibroids. It has a long recovery time; there is also a study shows 5% patients after myomectomy get infections because of the sutures[39].

UAE is a minimally invasive therapeutic approach to treat uterine fibroids. During the UAE procedure, physicians use x-ray fluoroscopy to guide a catheter to the uterine artery branch that supplies blood to the fibroid. Once the catheter is placed in the target artery, then the physician injects poly-vinyl alcohol-based particles which clog up the vessels that supply blood to the fibroid. The lack of blood supply to the fibroid is confirmed by x-ray fluoroscopy by injecting an x-ray contrast agent. Without a blood supply, fibroids necrose and shrink in size, leading to a minimization of symptoms. The procedure takes about 2-3 hours, and the UAE requires a relatively short recovery time (24-48 hours). Studies show that roughly 80% of the women who undergo UAE report improvement of their symptoms[40]. While the rate of complications following UAE is low, it is associated with complications such as infection, pre-mature menopause, amennorhea, and pain for several months. Furthermore, it is contra-indicated in patients who are allergic to iodine-based contrast agent.

Another non-invasive treatment method is FUS. In this method, an ultrasound transducer embedded within a water bath positioned outside the patient's body is used to focus high frequency (800 kHz – 1.5 MHz), high intensity sound waves on the target tissue of interest. The focusing of ultrasound is accomplished with either fixed curvature single-element transducers or via electronic steering of phased array ultrasound transducer. High intensity ultrasound is focused on tissue of interest and the resulting heat thermally ablates the tissue. Imaging techniques such as MRI (or ultrasound) are employed to monitor the temperature elevation at the ultrasound focus in real time during thermal ablation. With recent technological advances, the thermal dose delivery is

controlled based on real-time measurements of temperature using MRI- or ultrasound-based imaging techniques. The advantages of such FUS approaches are the non-invasive nature of the therapy, as well as comparatively short recuperation time. However, it should be noted that not all fibroids are amenable to FUS treatment. The size, location, and also the tissue character of the fibroids (such as tissue density, blood perfusion) will affect the treatment results. Studies have shown that certain types of fibroids with a high degree of perfusion as determined by MRI studies are difficult to treat with FUS[14, 41-42]. Furthermore, FUS treatments are time consuming. Many published studies show that typical treatment times for FUS can be on the order of 2-3 hours, during which patients have to lie still on the treatment table. So, to make FUS more effective, more research is needed. A more detailed discussion on the limitation of current FUS approaches for treating uterine fibroids is provided in Chapter 2.

1.3 INTRODUCTION TO MRgHIFU FOR UTERINE FIBROIDS

Magnetic resonance guided high intensity focused ultrasound (MRgHIFU) is the thermal therapy method using MRI to monitor temperature in real time while focused high intensity ultrasound is used to thermally ablate target tissues. MRgFUS has been used to treat a number of benign and malignant masses, such as uterine fibroids treatment[13-23], prostate cancer[43,44] , and liver cancer[45,46].

A typical MRgFUS involves three distinct steps. *Before treatment*, MR images are obtained to define the location and size of the fibroids, to aid in FUS treatment planning. Furthermore, some groups have used pre-treatment MR images to classify the fibroids into different types.

During treatment, MR images are obtained after every time the patient is moved to monitor the location of the fibroids and to guide the HIFU focus to the target treatment area. Real-time temperature map measurement is performed by MRI at slice locations around the HIFU focus as well as to monitor heat accumulation in the near field and far field to ensure patient safety. In some implementations, the thermal dose in the target area is calculated from the temperature maps, and the HIFU treatment is terminated automatically when a pre-defined thermal dose level is reached.

After treatment, MR images are acquired to determine treatment effectiveness. The closed loop interplay between MR imaging and therapeutic application of focused ultrasound has been an attractive feature of MR guided focused ultrasound surgery.

1.3.1 A brief introduction to MRI

Many textbooks discuss the phenomena of magnetic resonance in detail [47-49], and a cursory overview of the MR imaging will be provided in this sub-section.

Magnetic resonance image (MRI) is a non-invasive clinical imaging method. It is generated by the proton spin rotation in magnetic field. When there is no external field, magnetic dipoles distribute randomly in thermal equilibrium system. The relationship between magnetic moment and spin angular momentum is:

$$\vec{\boldsymbol{\mu}} = \boldsymbol{\gamma}\vec{\boldsymbol{J}} \qquad (\mathbf{1.3.1})$$

where μ is magnetic moment, J is spin angular momentum, and γ is gyromagnetic ratio. After applying an external magnetic field B, all the nuclear moments align in the

direction of external field. They can either be parallel or antiparallel to the external field. The relationship between magnetic moment and the external field is:

$$\frac{d\vec{\mu}}{dt} = \gamma\vec{\mu} \times \vec{B} \qquad (1.3.2)$$

As shown in Figure 1-4,

$$|d\vec{\mu}| = \mu \sin\theta \, |d\phi| \qquad (1.3.3)$$

$$|d\vec{\mu}| = \gamma|\vec{\mu} \times \vec{B}|dt = \gamma\mu B \sin\theta \, dt \qquad (1.3.4)$$

Then we get:

$$\omega = \left|\frac{d\phi}{dt}\right| = \gamma B \qquad (1.3.5)$$

where ω is the Larmor frequency.

In the human body, the MR signal is generated by the hydrogen nuclei. In a macroscopic system, the physical parameter that we can measure is the magnetization, which is represented by *M*. This *M* is the local magnetic moment per unit volume (V):

$$\vec{M} = \frac{1}{V}\sum_{\substack{protons \\ in\ V}} \vec{\mu_i} \qquad (1.3.6)$$

In an external magnetic field *B*:

$$\frac{d\vec{M}}{dt} = \gamma\vec{M} \times \vec{B} \qquad (1.3.7)$$

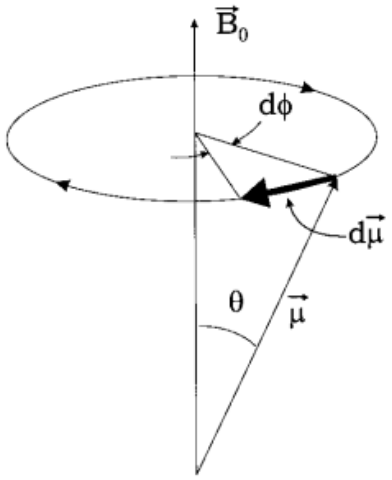

Figure 1-4 *Precession of Magnetic moment about an external magnetic field* B_o[47].

Usually the main external magnetic field B_0 is applied in the *z* direction. We call the *z* component of *M* (M_z) the longitudinal component of magnetization. To obtain an image, an additional external magnetic field (often referred to as B_1) is applied in the form of a radio-frequency wave (RF). B_1 is orthogonal to B_0 and rotates at Lamar frequency ω. The application of B_1 tilts *M* away from the direction of B_0. M_{xy}, which is the component perpendicular to B_0 called transverse magnetization, which generates the signal directly measured.

Unlike B_0 that exists over the whole scan duration, B_1 is applied for a very short time. After B_1 is removed, M_{xy} decays due to the inhomogeneity of the B_0 and the spin-spin relaxation, which will be introduced in the next section. We call this the free induction decay (FID,) and the envelope of FID is exponential (Figure1-5). Direct

measurement of FID is used in nuclear magnetic resonance (NMR) spectroscopy. To obtain an image for human body, we need more information.

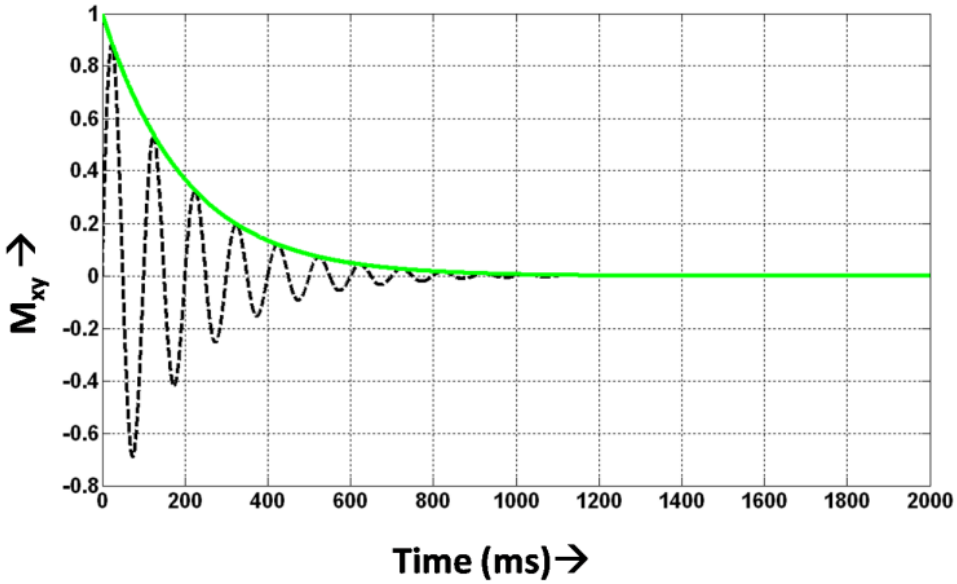

Figure 1-5 *FID and signal amplitude.The signal variation with time is FID and the envelope of FID is the signal amplitude.*

Spatial encoding process:

The FID does not have information about the spatial position of the spins. In order to resolve the spatial location of the spins, additional gradients are introduced in an imaging experiment to encode spatial position. For example, it would be desirable to form a two-dimensional image (2D-image) wherein the signal intensity at each spatial location is encoded in the received MR signal.

To obtain the information of the location for each interested voxel in human body, additional magnetic fields which linearly vary across the position (magnetic gradient, *G*) in three orthogonal directions are applied. These gradients can be used to encode the

spatial information. For example, following the application of additional magnetic field gradients of strength G_x and G_y along the x and y directions for a pre-defined duration (defined by the plane orthogonal to the main magnetic field ($\boldsymbol{B_o}$), which by convention is often referred to as the z-axis), the received MR signal s(t), contains spatial information, and may be written as: :

$$\boldsymbol{s(t) = \iint M_{xy}(x,y)\mathrm{e}^{-\mathrm{i}\gamma G_x \mathrm{x}\mathrm{t}}\mathrm{e}^{-\mathrm{i}\gamma G_y \mathrm{y}\mathrm{t}}\, dxdy} \qquad (\mathbf{1.3.8})$$

k space is introduced by:

$$\boldsymbol{\vec{k}(t) = \gamma \int_0^t \vec{G} d\vec{r}} \qquad (\mathbf{1.3.9})$$

Then we can get:

$$\boldsymbol{s(k_x, k_y) = \iint M_{xy}(x,y)\mathrm{e}^{-\mathrm{i}k_x \mathrm{t}}\mathrm{e}^{-\mathrm{i}k_y \mathrm{t}}\, dxdy} \qquad (\mathbf{1.3.10})$$

$S(k_x,k_y)$ is the Fourier transform of $M_{xy(x,y)}$. Thus, by an adequate sampling of k-space, one can obtain an estimate of the original object distribution $M_{xy}(x, y)$, by the inverse Fourier transformation of the received MR signal.

The received MR signal intensity is determined by a number of tissue-specific parameters (such as proton density, T_1 relaxation, T_2 relaxation, etc., discussed in the next section), as well as experimental parameters specific to the type of MR experiment performed (spin echo, gradient echo, etc.).

1.3.1.1 Spin-Spin Relation (T_2 Relaxation)

In the immediate aftermath of an application of an RF pulse to tip the longitudinal magnetization to the transverse plane, the spins in the transverse plane are coherent. But the intrinsic molecular motion or external magnetic field inhomogeneities results in the loss of phase coherence over time. The process of losing phase coherence is called dephasing. The dephasing purely caused by intrinsic molecular motion is due to spin-spin interactions and is often referred to as T_2 relaxation. T_2 is the true inter-molecular relaxation time. T_2 relaxation causes signal intensity to decay exponentially with time (Figure 1-7), and tissues with different local environments decay at slightly different rates. The signal intensity at time *t* is given by

$$\boldsymbol{s(t) = s_0 \exp\left(-\frac{t}{T_2}\right)} \qquad (\mathbf{1.3.11})$$

Usually, different tissues have different T_2 value; T_2 also decreases slightly as a function of main magnetic field strength. Table 1-1 shows T_2 value for some tissues under 1.5T and 3.0T.

The tissues with longer T_2 values decay less and appear brighter than ones with shorter T_2 values in T_2-weighted image (Figure 1-7a).

1.3.1.2 Spin-Lattice Relaxation (T_1 Relaxation)

Spin-lattice relaxation (T_1 relaxation) is a measure of the rate at which the energy absorbed by the spin system is lost to the surrounding (lattice) and regrows to thermal equilibrium following RF excitation. The MR signal regrowth toward thermal equilibrium is given by:

$$s(t) = s_0(1 - \exp(-\frac{t}{T_1})) \qquad (1.2.12)$$

Table 1-1 Spin-Spin relaxation time values of various tissues at 1.5T and 3.0T.

Tissue No.	Tissue	T_2 at 1.5T (ms)	T_2 at 3.0T (ms)
1	Blood	290 ±30	275 ±50
2	Muscle	44 ±6	50 ±4
3	Myometrium	117 ±14	79 ±10
4	Liver	46 ±6	34 ±4

Table 1-2 T_1 relaxation time values of various tissues under both 1.5T and 3.0T.

Tissue No.	Tissue	T_1 at 1.5T (ms)	T_1 at 3.0T (ms)
1	Blood	1441 ±120	1932 ±85
2	Muscle	1008 ±20	1412 ±11
3	Myometrium	1309 ±35	1514 ±156
4	Liver	586 ±39	809 ±71

In soft tissues, spin-lattice relaxation rates are different depending on the local environment; some typical T_1 values of various soft tissues are given below (Table 1-2). Unlike spin-spin relaxation time, spin-lattice relaxation times are strongly dependent on the main magnetic field strength. Higher main magnetic field will increase the T_1 values.

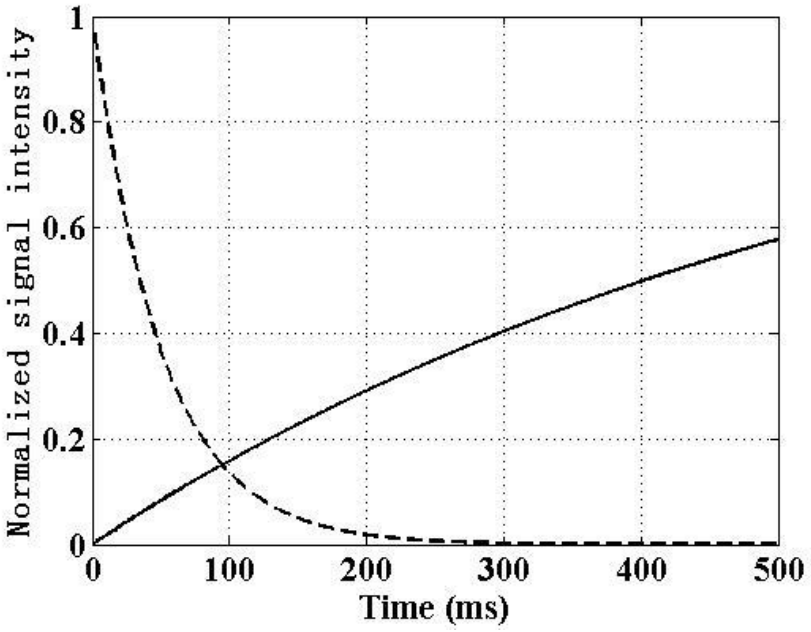

Figure 1-6 *Signal variation with time for T_2 decay and T_1 relaxation.The solid line shows signal intensity exponentially decays with time in T_2 decay. The dot line shows signal intensity exponentially increases with time in T_1 relaxation.*

In a typical MR experiment, this difference in the spin-spin and spin-lattice relaxation rates between soft tissues is exploited to create contrast between tissues, as well as between the normal and pathologic states of the tissues, by choosing appropriate experimental parameters such as echo time (TE) or repetition time (TR). It should be noted that for most soft tissues the T_1 relaxation times are an order of magnitude higher

than T_2 relaxation times (Figure 1-6). Typical T_1-weighted and T_2-weighted MR images of the brain are shown in Figure 1-7a and 1-7b respectively.

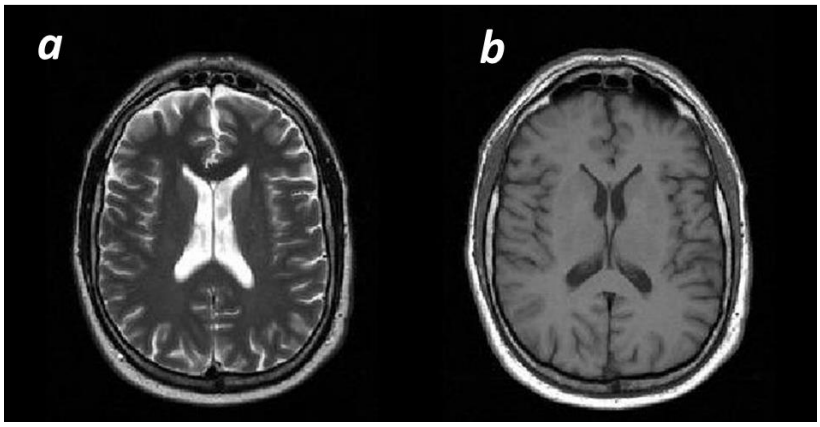

Figure 1-7 *T_2-weighted image and T_1-weighted image of brain. a.* T_2-weighted image of brain. CSF appears bright. b. T_1-weighted image of brain. CSF appears dark. CSF has longer T_1 and T_2 compared with the other brain tissues.

1.3.2 High Intensity Focused Ultrasound Therapy

Pressure waves at ultrasonic frequencies (~ 1 MHz) have traditionally been used as a medical imaging modality. An external ultrasound probe emits acoustic waves and makes an image from the ultrasonic reflections from tissue interfaces. Such images are typically used in obstetric and gynecologic examinations, or in cardiovascular applications to evaluate heart and valvular function. Ultrasound waves propagating within tissues are scattered at tissue interfaces, and the energy is lost due to absorption and scattering. In diagnostic imaging applications, the applied ultrasound energy is too minuscule to cause tissue damage. However, at sufficiently high power levels,

ultrasound propagation can result in tissue damage via thermal effects (heating) or mechanical rupture of cells.

However, both of these effects (thermal and mechanical) can be harnessed for patient benefit. For example, the absorption of focused ultrasound energy in the target region can be used to thermally ablate tumors of the breast, liver, prostate, uterus, etc., or for palliative treatment of bone metastasisor for local drug delivery. The mechanical effects associated with high intensity focused ultrasound can be used to measure the local tissue mechanical properties, eg., the measurement of the speed of shear-wave propagation and recent studies show that diffuse diseases such as liver fibrosis can be evaluated by MR elastography[50-52]. In the next section, we provide a brief outline of the HIFU equipment.

1.3.2.1 MRgHIFU equipment

The ultrasound is normally generated by applying RF voltage across a piezoelectric materials, which expands and contracts in proportion to the applied voltage. Such piezoelectric materials include quartz and lithium niobate. Quartz crystals, which have narrow peaks, have largely been replaced by ferroelectric ceramics such as lead zirconate titanate (PZT).

To generate a focused field, the simplest method is to use a single element spherical curved shell of piezoelectric or piezoceramic material. But in practice, phased arrays are used instead of single element shell. The phased arrays are usually formed by many individual elements on the spherical surface (Figure1-8)[53].

One commercially available MRI-compatible device that we used in this study is Sonalleve^{TM} (Philips Medical Systems, Vantaa, Finland). It has multi-elements transducer containing 256 elements with 6.6 cm diameter which are on a spherical shell. The radius of curvature of transducer is 12 cm and the aperture is 13 cm. Ultrasound with 1.2 MHz and 1.4 MHz can be generated by this transducer.

The MR scanner combined with HIFU used in this study is 1.5T scanner (Achieva, Philips Medical System, The Netherlands).

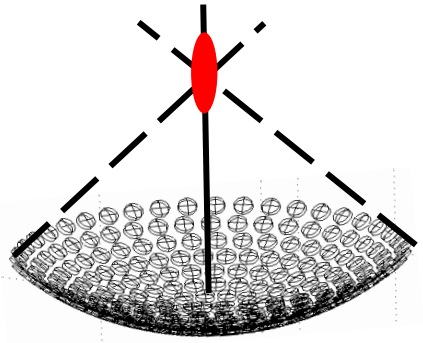

Figure 1-8 *spherical phase-array electrical focusing transducer and the ultrasound beam focus.*

1.3.2.2 Volumetric heating algorithm

A new volumetric heating algorithm in which the ultrasound focal point dynamically moves along the pre-defined trajectories during heating was introduced[54]. Such pre-defined trajectories are consisted of multiple outward-moving concentric circles (Figure 1-9). For each circle, several points are set. During heating, ultrasound focus moves from one point to another.

It is shown clearly in Figure 1-9 that the ultrasound focus moves in certain trajectories during heating. An ellipsoid shape volume with long axis along the ultrasound transfer direction is heated. This heated volume is called a treatment cell. Four different sizes of treatment cells can be generated by the system, including 4 *mm*, 8 *mm*, 12 *mm*, and 16 *mm* which are the lengths of short axes of the treatment cells.

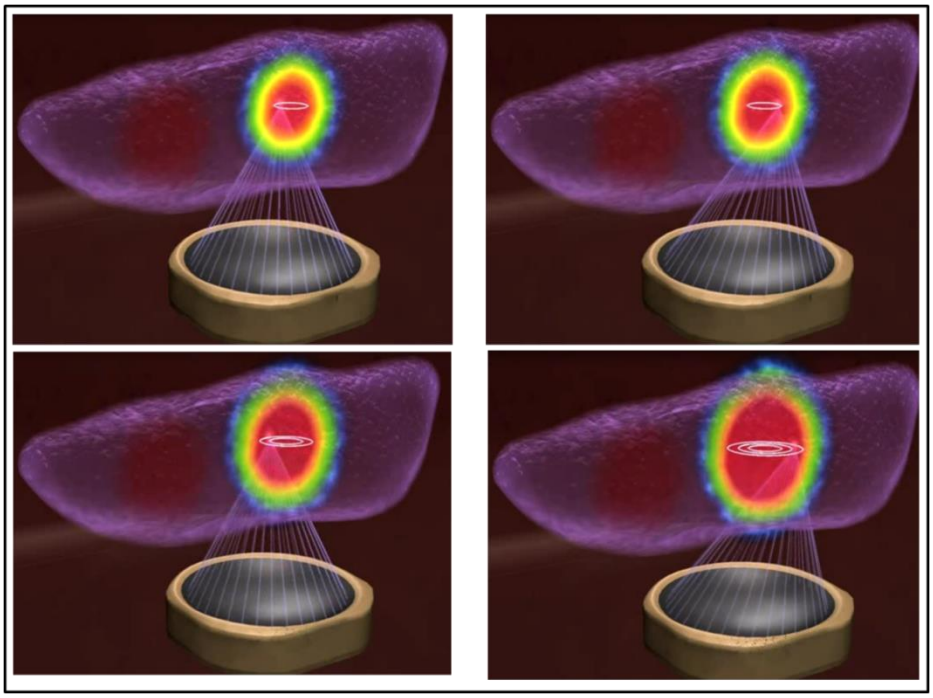

Figure 1-9 *Volumetric sonication.The colored volume shown inside the tissue (blue surrounding region) is the heating volume.*

Real-time temperature maps are measured by the MR scanner, and thermal dose is simultaneously calculated by the HIFU console. Two heating modes are supplied by the system. One is called the fixed treatment cell. In this mode, the heating time is planned and fixed before treatment. The other one is called the feedback treatment cell. Heating is

stopped when the outermost sub-trajectory reached the target temperature or alternatively all voxels in the entire treated volume reaches a thermal dose of tissue necrosis (240EM).

1.3.3 MRgHIFU treatment procedure of uterine fibroids

Before treatment:

The MR image acquisitions required before treatment including: survey scan, skin bubble and scar scan, and T_2-weighted images.

(1) Prediction before treatment

Current studies show that not all the fibroids can be successfully treated. The skin surface situation, location, and size of fibroids all determine whether MRgHIFU is a proper choice for therapy.

To avoid the high energy caused by the ultrasound reflection at the surface of two not continuous tissues, patients should not have scars on the abdomen and also no bubbles between the skin and gel pad. Also, the ultrasound cannot pass through the bladder or bowel.

The equipment limitation determines that the only the tissue depth less than 10cm can be heated. Thus the distance between the abdomen skin surface and the center of the fibroid cannot be deeper than 10cm.

The size of the fibroids is very important in the MRgHIFU therapy. Usually the final dead volume after treatment is bigger that the sonication planning volume, so for safety purposes, the sonication treatment cell should not be set at the edge of the fibroid.

This means the volume of the fibroids cannot be too small. However, the fibroids cannot be too large either. That is because considering the benefit of the patients, more than 50% of the total volume of the fibroids must be treated. So the volume of qualified fibroids should be smaller than 250 *ml* and the diameter of the fibroid should be bigger than 30 *mm*.

Whether the fibroids can be treated is also determined by the tissue character of the fibroids. There are studies classified uterine fibroids into different types based on T_2-weighted images. Based on the signal intensity of the fibroids compared with muscle and myometrium in T_2-weighted image, fibroids can be classified into 2 types, 3 types, and 5 types. The 3-type classification is most popular in the MRgHIFU therapy for uterine fibroids. In T_2 weighted image, compared with signal intensity of muscle and myometrium, type I fibroids have lowest signal intensity (comparable with muscle), type II fibroids have medium signal intensity (higher than muscle but lower than myometrium), and type III fibroids have the highest signal intensity. Researchers found that HIFU only works successfully on type I and type II fibroids but not on type III fibroids. Some researchers claimed this may be because high blood perfusion in type III fibroids. More details will be introduced in Chapter 2.

(2) Patient position and treatment cells planning

T_2-weighted images are obtained to define the location of the fibroids (Figure 1-10). The treatment cells are planned based on these T_2-weighted images. If it is necessary, patients are moved multiple times to position the fibroids inside the treatment window of

the ultrasound. For some patients, bladder or rectum injection is required to force the fibroids move to the treatable location. After every movement or injection, a T_2-weighted image is acquired to locate the fibroids.

Figure 1-10 *Treatment cell planning on T_2-weighted image. The MRI is the sagittal view of uterine fibroid. The two orange triangles are the ultrasound pass way of ultrasound beam. The orange ellipsoids inside the fibroid are the treatment cells. The white contour shows the region with thermal dose equal or bigger than 240 EM while the orange contour shows the region with thermal dose equal or bigger than 30 EM.*

<u>During treatment:</u>

During treatment, temperature mapping of six slices is performed during heating. The corresponding thermal dose maps are calculated in real time and shown in the HIFU consol. These six slices include three slices with coronal view located on the treatment cell with the middle slice crossing through the center of treatment cell. One slice with

sagittal view crosses through the center of the treatment cell. The other two slices are used to monitor the near-field and far-field temperature, both of which are coronal view.

After treatment:

It is known that after treatment, tissue blood perfusion significantly reduces in the treated region. Gd^{3+}-based contrast agent is injected into human body to shorter T_1 of the blood. The tissues with blood perfusion appear bright, while the tissues without blood perfusion appear dark. Thus the treated volume in the fibroids appears darker than the non-treated volume and this darker volume is called non-perfused volume (NPV). In MRgHIFU therapy, the NPV is used to estimate of the treatment result.

1.3.4 The benefit and challenges of MRgHIFU treatment compared with other therapy methods

Compared with invasive uterine fibroids surgeries, such as hysterectomy and myomectomy, MRgHIFU is much safer. No infection would happen during surgery. The recovery time is also very short. Compared with UAE, which is also a non-invasive therapy method for uterine fibroids, research showed that patients have more chance for pregnancy after MRgHIFU. So MRgHIFU may be a better choice for the patients who still want to pregnant after uterine fibroids treatment. Besides, it is also a good choice for the patients who are allergy to the iodine-based contrast agent required in UAE therapy. For all the reasons mentioned above, MRgHIFU have already attracted much interest of researchers. However, like any other therapy methods, there are many chanllenges in MRgHIFU. It will be discussed in the next chapter.

2 CURRENT WORK AND CHALLENGES TO MRgHIFU THERAPY OF UTERINE FIBROIDS

Compared with other therapy method of uterine fibroids, MRgHIFU has a lot of advantages, such as non-invasiveness and short recovery time, but there are still several challenges.

The two primary challenges of MRgHIFU therapy of uterine fibroids are: (1) the efficiency of treatment is low, and (2) not all the fibroids can be treated by HIFU therapy.

Researchers are trying to minimize the limitations generated by these challenges. In this chapter, we will discuss how people have tried to improve the treatment efficiency and treatment efficacy of MRgHIFU therapy of uterine fibroids. At the end of this chapter, there is a brief introduction of the aims and hypothesis of this dissertation, which is how to deal with all the challenges.

2.1 LOW TREATMENT EFFICIENCY OF MRgHIFU THERAPY OF UTERINE FIBROIDS

In Chapter 1.3.3, the process of the MRgHIFU treatment of uterine fibroids was introduced. The total treatment time includes patient set up time, scan time, and heating time. In the current study, the total treatment time is limited into 3 hours. This is because patients are required to lie on the treatment table and not move during the whole treatment process. A long treatment time will cause patients feel uncomfortable. Besides, it can also cause blood vessel blockage which is very dangerous.

2.1.1 Why the treatment has low efficiency

2.1.1.1 Time wasting for patients position planning

As it was mentioned, to make sure the fibroid is in the treatment window, patients may be moved for several times before and during the treatment. A T_2 planning image is required after each movement. Usually, each T_2 planning image takes about 5 min,so the total planning time is long. Thus the time left for the thermal therapy is shortened. This will reduce the treatment efficiency.

2.1.1.2 Time wasting during sonication

During thermal therapy, a test shot is applied at the very beginning to determine the proper treatment heating power. Usually feedback cells are used. The inhomogeneity of the fibroids makes the sonication time varies from one region to another region. The region with higher perfusion requires longer sonication time. This long time can be shortened by increasing the treatment power. However, it will waste more time if a test shot is applied before every treatment cell.

2.1.2 Current work to improve the treatment efficiency

2.1.2.1 How to reduce the scan time

There are several methods to reduce the scan time, including partial Fourier technique[55,56], fast imaging techniques[57,58] , and parallel imaging techniques[59,60].

Introduction to spin echo sequence

In MRgHIFU treatment, T_2-weighted planning image is acquired by a spin echo (SE) -based sequence.

In SE sequence, two RF pulses are applied, a 90° pulse followed by a 180 °pulse. The 90° pulse is called excitation pulse. It is applied along the *x* axis at *t* = 0. The magnetization is tipped to transvers plane and all the spins point along the *y* axis. The spins start to dephase, and the phase accumulation in the rotation frame is

$$\boldsymbol{\phi(\vec{r},t) = -\gamma\Delta B(\vec{r})t} \qquad \boldsymbol{0 < t < \tau} \qquad (\mathbf{2.1.1})$$

After time τ, the 180° pulse is applied along *y* axis, and this pulse is usually called the refocusing flip angle. All the spins are rotated by 180° along *y* axis. The accumulated phase turns into:

$$\boldsymbol{\phi(\vec{r},\tau^{+}) = \gamma\Delta B(\vec{r})\tau} \qquad (\mathbf{2.1.2})$$

All spins start to rephase after that, so the phase accumulation is equal to:

$$\boldsymbol{\phi(\vec{r},t) = \phi(\vec{r},\tau^{+}) - \gamma\Delta B(\vec{r})(t-\tau) = \gamma\Delta B(\vec{r})(t-TE)} \qquad \boldsymbol{t > \tau} \qquad (\mathbf{2.1.3})$$

in which TE is equal to 2*τ*. A so-called echo is formed at this time point, and this TE is called the echo time. Equation 2.1.3 shows when *t* = TE, the accumulated phase is 0. Signal intensity is measured at this time point. In the SE sequence, only T_2 introduces the signal decay, the inhomogeneity of the external field does not have any effect. It is

worthy knowing that during all the acquisition, TE is the time point when the center of *k* space is filled. So, TE affects the image signal intensity.

Introduction to *k* space

As it was mentioned in Chapter one, MR image is the Fourier transform of a signal data matrix called *k* space, so the characters of image such as scan time, signal intensity, and the contrast between the interested tissues are all determined by *k* space.

To understand how *k* space works, we take a 2D image for an example. In 2D imaging acquisition, there are two directions in *k* space, the k_x direction and the k_y direction. The signals filled in the k_x direction are determined by the readout encoding, while the signals filled in the k_y direction are determined by phase encoding (Figure 2-1).

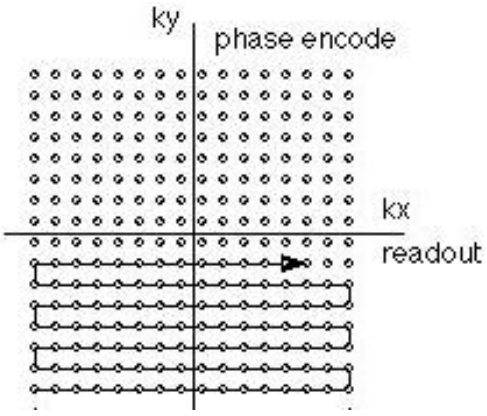

Figure 2-1 *An example of 2D k space. k_x is readout phase encoding direction and k_y is phase encoding direction*[47].

The signal intensity of the image is determined by the signal filled in the center of the *k* space, while the spatial resolution of the image is determined by the signal filled at the edge of the *k* space. The *k* space with a high signal in both the center and the edge

generates a high signal intensity and a high spatial resolution image. Besides, the signal profile in phase encoding direction will also affect the spatial resolution of the image. The less variation of the signal in the phase encoding direction, the higher the spatial resolution of the image. Figure 2-2 shows the simulation image of a digital phantom under different phase encoding signal profiles.

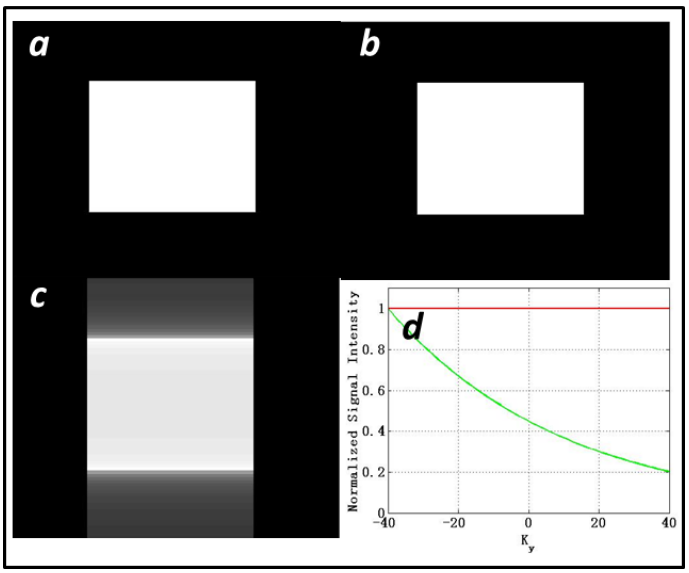

Figure 2-2 *Effect from signal profile to the image (Digital phantom simulation). a. Digital phantom with T_2 = 50ms; b. MR image for digital phantom generated by multi-shot (msh) TSE sequence; c. MR image for digital phantom generated by single-shot (ssh) TSE sequence; d. Signal profile in k_y (phase encoding) direction of msh-TSE (red) and ssh-TSE(green) sequence.*

Conventional techniques to reduce scan time

During one readout, one line in the *k* space along the k_x direction is filled. So the acquisition time is determined by how long it takes to fill all the signals in the k_y direction of the *k* space:

$$t_{scan} = TR * n_{phase\_encoding} \qquad (2.1.4)$$

TR is the repetition time, which is the time duration between two following excitation flip angles.

Partial Fourier technique

To reduce the acquisition time, a partial Fourier technique was introduced. The basic idea of the partial Fourier technique is that instead of filling the whole *k* space, the k_y direction is the only part that is filled. A parameter called half scan factor, which stands for the ratio of the filled *k* space, was introduced. The acquisition time is equal to:

$$t_{scan} = h_{half\_scan\_factor} * TR * n_{phase\_encoding} \qquad (2.1.5)$$

As long as the center of *k* space is filled by the same signal, the intensity of image would not change. However, the half scan factor will affect the spatial resolution of the image because no signal is filled at the edge of *k* space. The half scan factor cannot be too small, i.e. it must be bigger than 0.5.

Fast imaging technique

Another way to reduce acquisition time is using a fast imaging technique. In the fast imaging technique, instead of only fill one line per shot in *k* space, serval lines are filled. The number of lines filled per shot is called fast scan factor. The SE sequence associated with fast imaging technique is called fast spin echo (FSE) or turbo spin echo (TSE) sequence, and the fact scan factor is called FSE or TSE factor (Figure 2-3).

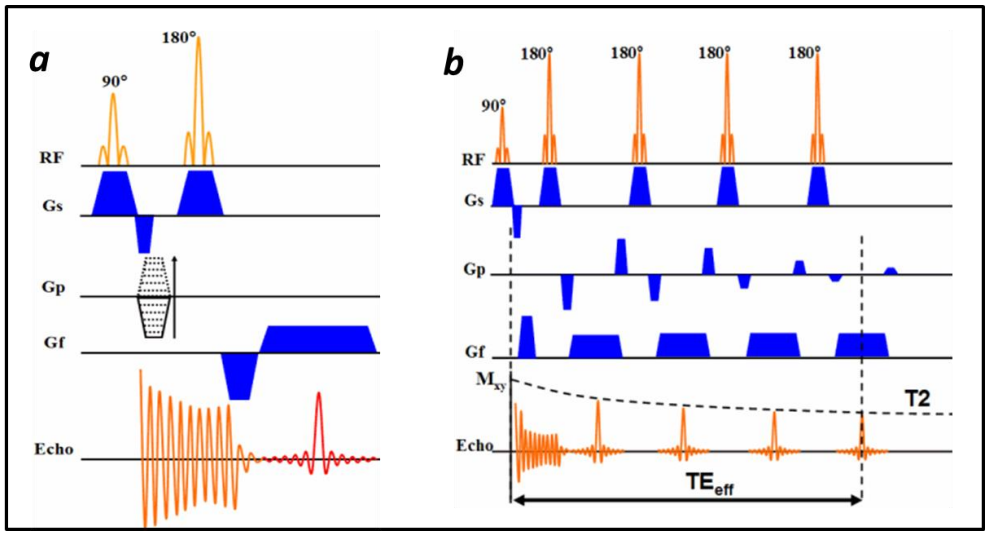

Figure 2-3 *Spin echo (SE) sequence and Turbo spin echo (TSE) sequence. a. SE sequence. b. TSE sequence with TSE factor: 4. http://www.revisemri.com/questions/pulse_sequences/tse*

In the fast imaging sequence, the *k* space is separated into several segments, with the number of segments equal to the fast imaging factor. For example, if the fast imaging factor is *n*, which means in every shot, *n* signals are collected and filled into *n* segments of the *k* space with one signal per segment. Besides, the signals obtained in the same shot are filled in the same location of each segment, which means if the first signal obtained is filled in the first line of its corresponding segment, all the other signals obtained in the same shot will also be filled in the first line of their corresponding segment (Figure 2-4).

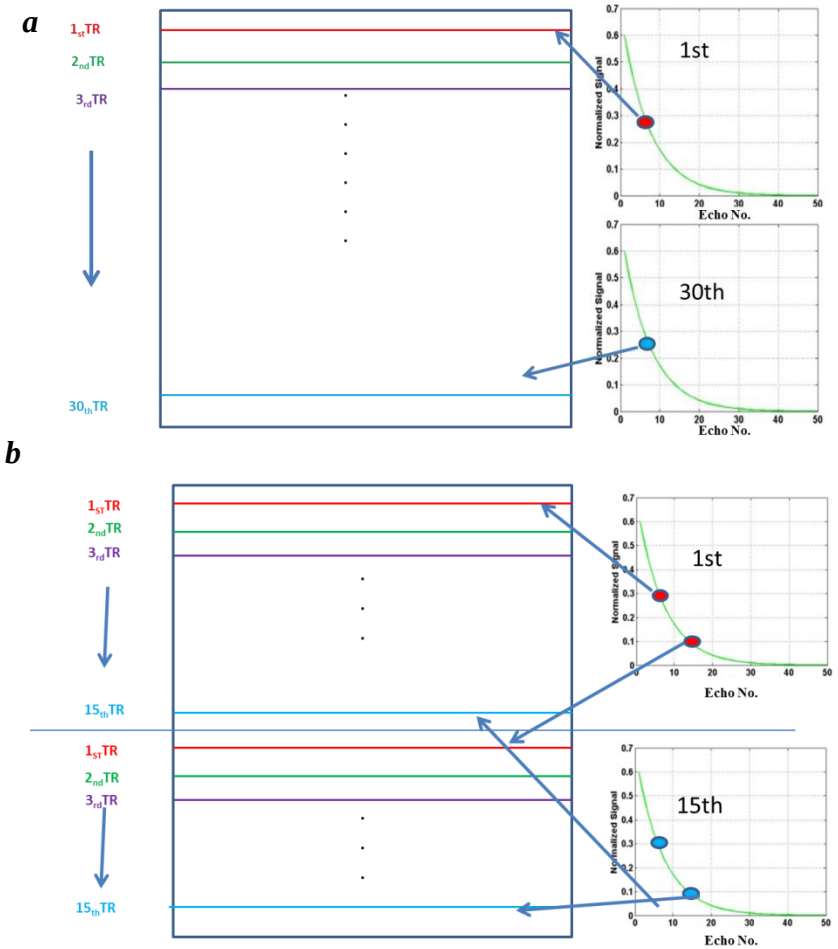

Figure 2-4 *Example of phase encoding in SE and TSE sequence. a. Phase encoding in SE sequence. All 30 signals filled in k space are the same. b. Phase encoding in TSE sequence with TSE factor 2. k space is split into several segments. Signals in the same segment are the same. Signals in different segments are different. k space is a 30 by 30 matrix.*

One extremely situation of fast imaging sequence is single shot (ssh) sequence, in which the whole *k* space is filled in only one shot. So in single shot sequence, scan time is

equal to TR. The acquisition finished in several TR is called multi-shot (msh) sequence. The acquisition time is equal to:

$$t_{scan} = \frac{n_{phase\_encoding}}{TSE_{factor}} * TR \qquad (2.1.6)$$

However, like the partial Fourier technique, the fast imaging technique also introduces problems that reduce the image quality. First, more than one signal are acquired in one shot, so signals in the k_y direction are not the same due to T_2 decay. The signal profile in the phase encoding direction affects the image resolution. The faster the signal varies along the phase encoding direction, the poorer the image quality. This means the tissues with short T_2 have poor spatial resolution images, and images will also have lower spatial resolution when an ssh sequence is applied. Second, a TSE sequence requires a longer TE than a SE sequence, so SNR is lower in an image acquired by a TSE sequence. And last, a TSE sequence has a high specific absorption rate (SAR) if many 180° refocusing angles are applied in a short time. So it is not realistic to use a TSE sequence with a very high TSE factor to reduce the scan time.

Parallel image technique

For the scanner with a multi-channel coil, a method called the parallel image technique was introduced to reduce the acquisition time. SENSE is one of the parallel image techniques which are widely used. In the sequence with application of SENSE, each channel only images one part of the object; however, the image is then reconstructed

using the information obtained from all the channels, and the final image is the image for the whole object. In SENSE application:

$$t_{scan} = TR * \frac{n_{phase\_encoding}}{s_{SENSE_{factor}}} \qquad (2.1.7)$$

A parameter called SENSE factor was introduced. It shows how much acquisition time reduced. So the higher the SENSE factor is, the shorter the acquisition time is. However, the signal to noise ratio (SNR) is affected by SENSE factor. The relationship between SNR and SENSE factor is:

$$SNR_{pos} = \frac{SNR_{pre}}{\sqrt{s_{SENSE_{factor}}}} \qquad (2.1.8)$$

so the high SENSE factor causes a low SNR.

In the current T_2-weighted imaging protocol performed in MRgHIFU, all three techniques are applied (Equation 2.1.9). However, the scan time is still long (about 5 min).

$$t_{scan} = \frac{n_{phase\_encoding}}{TSE_{factor} * s_{SENSE_{factor}}} * TR * h_{half\_scan\_factor} \qquad (2.1.9)$$

2.1.2.2 How to improve the sonication efficiency

During sonication, shortening sonication time for each treatment cell and using fewer treatment cells to obtain more NPV can improve sonication efficiency.

Liu et al. reported the high perfused region in fibroids required higher acoustic power to confer effective treatment via MRgHIFU. The dynamic contrast enhanced (DCE)

image was applied, and the K^{trans} map was analyzed one day before treatment[61]. It showed that K^{trans} map was a good tool to guide the acoustic power setup. It can help people avoid the waste of time caused by the low acoustic power applied to high perfused region.

Voogt et al. reported that ablation of the feeding blood vessel of fibroids can improve the treatment efficiency[62]. In the study, not only the fibroids were heated by ultrasound, but also the blood vessels feeding the fibroids were ablated by sonication. The results show that the final NPV was 4.3 (patient 1) and 2.3 (patient 2), times higher than the expected value calculated based on the thermal dose distribution.

However, there is one limitation of these two studies, which is both of them involved contrast agents involved. Because the contrast agent is not stable under high temperature, the therapy had to be performed the next day after perfusion measurement. Besides, the patients with dysfunctional kidney cannot use these methods.

Kim et al. introduced a new treatment strategy called one layer strategy to improve the treatment efficiency[63]. All the treatment cells were planned on the same coronal plane at a depth of half to anterior, two-thirds of the anteroposterior dimension of fibroids. The NPV for 27 fibroids was 64.2% of the whole volume of the fibroids which was larger than the expected volume calculated based on the thermal dose distribution.

This one layer strategy is non-contrast involved, but the reason why this strategy introduced the improvement of treatment efficiency is unclear. It may be caused by the

near field heating accumulation or secondary effect of heating. If this reason can be found out, this strategy could bring more benefits.

2.2 NOT ALL THE FIBROIDS CAN BE TREATED BY MRgHIFU METHOD

2.2.1 Fibroid classification

Clinical results show that not all the fibroids are treatable by HIFU therapy. Funaki et al. classified uterine fibroids into 3 types based on the contrast between muscle, fibroids, and myometrium in T_2-weighted images[14]. Type I fibroids have the comparable signal intensity with muscle; Type II fibroids have the medium signal intensity; while Type III fibroids have highest signal intensity (Figure 2-5). Because both Type I and Type II fibroids are treatable, in some studies, fibroids were classified into only two types[64]: hypointensity fibroids (Type I and Type II fibroids) and hyperintensity fibroids (Type III fibroids).

Figure 2-5 *Funaki classification of uterine fibroids[14]. a. Type I fibroid (signal intensity of fibroid is comparable with muscle.) b. Type II fibroid (signal intensity of fibroid is higher than muscle but lower than myometrium.) c. Type III fibroid (signal intensity of fibroid is higher than myometrium.)*

Zhao et al. reclassified the fibroids into 5 types[41] (Figure 2-6). This new classification splits Type III fibroids in the Funaki classification into 3 types based on the tissue homogeneity. Clinical results showed that only the slightly homogenous hyperintense fibroids were difficult to be treated. In Zhao et al's another work, fibroids were classified into 4 types which was including hypointense, isointense, homogenous hyperintense, and heterogeneous hyperintense fibroids[65]. Among all kinds of fibroids, homogenous hyperintense fibroids were the most difficult to be treated.

2.2.2 Current work on the investigation of the untreatable fibroids

As it is known, in thermal therapy, the treatment result is determined by many factors, such as absorption coefficient, thermal conductivity, and blood perfusion. Many studies have been done to investigate the character of untreatable fibroids.

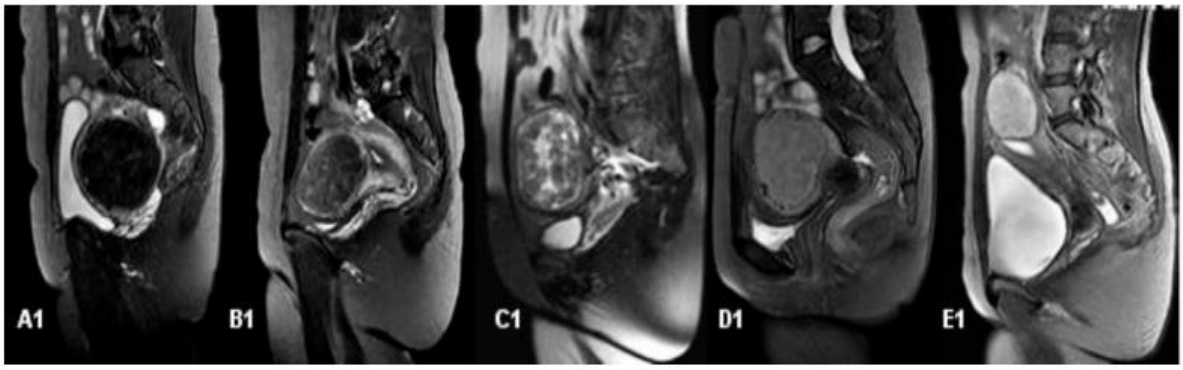

Figure 2-6 *Zhao classification of uterine fibroids[65]. A1. Hypointense. B1. Isointense. C1-E1, hyperintoense: C1 is heterogeneous; D1-E1 are homogeneous, D1. Slightly homogeneous hyperintense fibrods; E1. Markedly homogenous hyperintense fibroids*

Pathologic studies show that homogenous hyperintense fibroids can be structurally different, and the treatment response may be determined by underlying tissue properties such as density, moisture content, and collagen content[65].

There are also some studies focused on the diffusion and perfusion microstructure investigation of fibroids. Kim claimed that the reason why Type III fibroids are untreatable is because the high blood perfusion. But only in one paper was K^{trans} measured, and it included only 2 type III fibroids [42]. Wang et al. and Ikink et al. applied the intravoxel incoherent motion (IVIM) model to obtain estimations about tissue microstructure, as well as microcirculation of different types of fibroids classified by Funaki classification[66,67]. They found the diffusion coefficient (*D*) were different, but no significant difference on blood volume ratio (*f*) or perfusion coefficient (*D**) between different types of fibroids. This observation is in contrast to DCE-MRI-based characterization of fibroids, which suggests that Type III fibroids are highly vascular and well perfused.

2.3 LIMITATION CAUSED BY THE CONTRAST AGENT

In MRgHIFU, CE image is applied to measure the NPV which is used to estimate the treatment result. This contrast-involved method cannot be used for the patients who have abnormal kidney function, thus these people cannot be treated by MRgHIFU.

Many studies have reported a discrepancy between the fibroid treatment volume as assessed by thermal dose maps, and the NPV. Non-contrast alternatives using DIFFUSION WEIGHTED IMAGING(DWI)[68-72], apparent diffusion coefficient (*ADC*) map[68-71] , and ^{23}Na MRI have been tested as means of monitoring the progress of MRgHIFU therapy[68]. ^{23}Na MRI requires specialized hardware, and is not widely available. In DWI, NPV appears brighter than the non-treated region, and it overlapped with the NPV in CE image and thermal dose (TD) map very well. But the DWI reported

in the previous work had low SNR. The NPV has high *ADC* value compared with the non-treated region, but there is not clear edge between these two tissues which introduces trouble to measure the NPV.

2.4 SPECIFIC AIMS AND HYPOTHESIS

In this dissertation several goals have been achieved:

(1) Develop a modified T_2-weighted image sequence to decrease the scan time.

Hypothesis 1: Variable refocusing flip angles associated with ZOOM technique will shorten scan time, and increase SNR and CNR.

(2) Investigate the tissue microstructure and microcirculation for different types of fibroids classified by Funaki classification. Find out the perfusion and diffusion difference between Type III fibroids and other treatable fibroids. Find out the reason why no significant perfusion difference for Type III fibroids reported in previous studies.

Hypothesis 2: f-value is significantly different from one type of fibroids to another ($f_{TypeIII} > f_{TypeII} > f_{TypeI}$). The reason why this difference was not observed in the published work is because T_2 decay effect was not taken into account.

(3) Develop a new no-contrast agent involved NPV estimation tool which satisfies: (i) non-contrast agent involved (ii) high SNR and CNR.

Hypothesis 3: DWI and f_c (f with T_2 correction) map can be used as no-contrast agent involved NPV estimation tool. Instead of high b value DWI reported by the published work, low b value DWI has high SNR and CNR

between treated region and non –treated region. So low b value DWI is a better choice.

(4) Investigate the tissue microstructure response to heat during sonication by studying the IVIM model.

Hypothesis 4: D various with temperature, but it cannot be applied as a biomarker to test the tissue damage for the tissue with low f. f varies with temperature when the tissue microstructure changes after certain temperature.

3 DIFFUSION WEIGHTED IMAGING (DWI) AND INTRAVOXEL INCOHERENT MOTION (IVIM) MODEL APPLICATION IN MRgHIFU OF UTERINE FIBROIDS

As it was mentioned in Chapter 2, DWI and IVIM model can be applied in the tissue microstructure studies which is including both diffusion and perfusion information. In this chapter we will discuss how to solve the challenge of application of DWI and IVIM in MRgHIFU therapy of uterine fibroids introduced in Chapter 2.

3.1 INTRODUCTION TO DIFFUSION WEIGHTED IMAGING (DWI) AND INTRAVOXEL INCOHERENT MOTION (IVIM) MODEL

3.1.1 DWI

In MR scanning, when the extra external magnetic field *G* is applied, the phase accumulation introduced by the precession of the transverse magnetization of spins under *G* at location *r* over time *t* is:

$$\boldsymbol{\phi = \int_0^t \omega\, dt = \phi_0 + \gamma \int_0^t G \cdot r\, dt \;=\; \phi_0 + \gamma \int_0^t v(t) \cdot G(t) \cdot t\; dt} \quad (\mathbf{3.1.1})$$

where ϕ_0 is the phase accumulation by spins at $r = 0$. It is clear that spin motion (not precession) can be described by the phase change during time. So the diffusion of the spins can also be measured by MRI. In diffusion weighted imaging (DWI), the same gradient is applied before and after the refocusing pulse (Fig 3-1).

The phase accumulation introduced by the first gradient of the non-diffused spins is cancelled by the phase accumulation introduced by the second gradient. Only the phase

accumulation of the diffused spins is left. As we know that the phase decreases the net transverse magnetization, so the diffused tissue appears darker in the DWI.

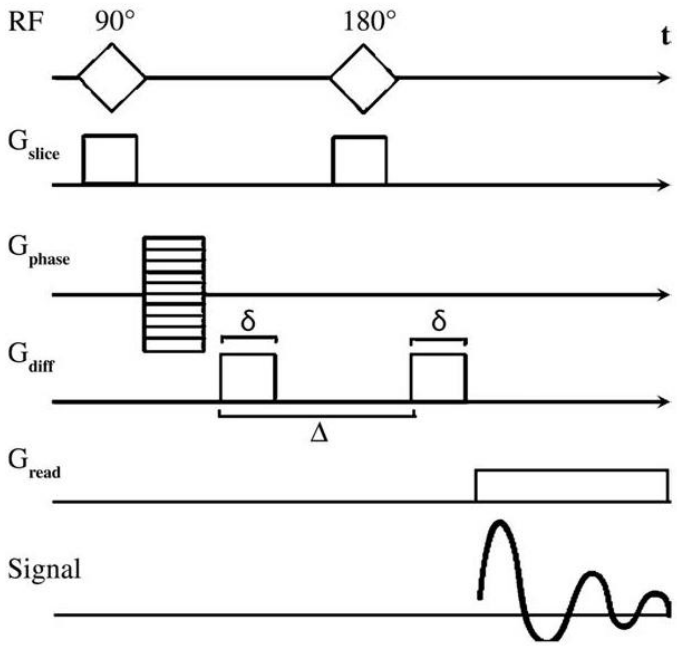

Figure 3-1 *DWI sequence. DWI sequence: δ is the length of diffusion gradient, and Δ is the time duration between two diffusion gradients. The two diffusion gradients applied before and after the 180° refocusing angles are exactly the same.*
http://radiopaedia.org/images/2987636

3.1.2 IVIM model

In 1988, Le Bihan et al. introduced a new model to describe both perfusion and diffusion inside tissue, which is called intravoxel incoherent motion (IVIM) model[73]. The model is based on the DWI obtained by SE sequence. It assumes that the signal intensity in DWI is constructed by two parts: one is diffusion of the pure tissue, and the other one is the perfusion and diffusion of blood.

As it is known, diffusion introduces signal exponential decay in DWI (Equation 3.1.2).

$$\boldsymbol{s(b) = s(0) \cdot e^{-b \cdot D}} \qquad (\mathbf{3.1.2})$$

in which *b* is called diffusion gradient factor, determined by the strength (*G*) and duration (δ) of the diffusion gradient, and as well as the time interval (Δ) between two diffusion gradients. The unit of *b* is *s/mm*^{2}:

$$\boldsymbol{b = \gamma^2 \cdot G^2 \cdot \delta^2 \cdot \left(\Delta - \frac{\delta}{3}\right)} \qquad (\mathbf{3.1.3})$$

Bihan et al. assumed that the blood in the small vessels flows to no specific direction because the vessels themselves go to every direction. So from macroscopic view, the blood perfusion acts like diffusion, and it is called pseudo diffusion (**Figure 3-2**).

Then the signal decay introduced by perfusion should have similar formula with diffusion, as it is shown in Equation 3.1.4.

$$\boldsymbol{s(b) = s(0) \cdot e^{-b \cdot D^*}} \qquad (\mathbf{3.1.4})$$

*D** is the perfusion coefficient. So the signal intensity in DWI is:

$$\boldsymbol{s(b) = (1 - f) \cdot s_{tissue} + f \cdot s_{blood}} \qquad (\mathbf{3.1.5})$$

$$\boldsymbol{s(b) = s_0 \cdot \left((1 - f) \cdot e^{-b \cdot D} + f \cdot e^{-b \cdot (D + D^*)}\right)} \qquad (\mathbf{3.1.6})$$

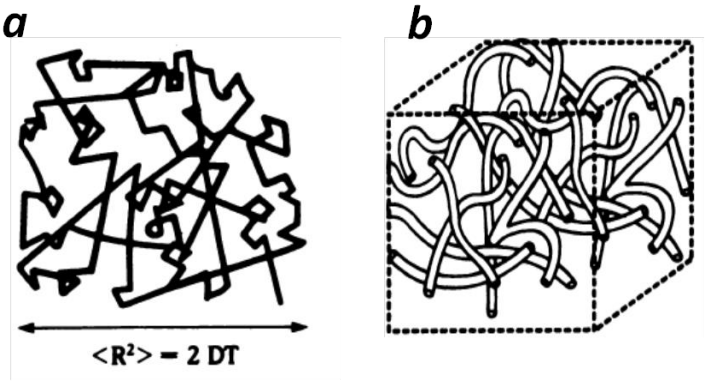

Figure 3-2 *Diffusion and perfusion inside tissue. a. Molecule diffusion. b. Blood perfusion (pseudo diffusion)*[73].

Equation 3.1.6 is the basic formula of IVIM model, in which *f* is the volume ratio of blood with value range from 0 to 100%. *D* is the diffusion coefficient representing how fast the Brownian motion of the water molecule in pure tissue, while *D** is the perfusion coefficient representing how fast the blood flows. Both the unit of *D* and *D** is mm^2/s. IVIM model can be applied to different region of human body. For example, it is used in liver lesion study[74,75], investigation of breast cancer[76,77] and prostate cancer[78,79].

To calculate the three parameters in the IVIM model, a set of DWI with different *b* values are required. The two common methods to calculate *D*, *D** and *f* are bi-exponential fitting and asymptotic fitting.

3.1.2.1 Bi-exponential fitting of IVIM model

Bi-exponential fitting is the basic data analysis method of the IVIM model. The signal intensities and corresponding *b* values are applied to Equation 3.1.6, and then *D*, *D**, and *f* is obtained.

3.1.2.2 Asymptotic fitting of IVIM model

Bi-exponential fitting of IVIM model can generate reasonable results, but not under all the conditions, Pekar et al. reported in the study in 1992, that when *f*<5%, bi-exponential fitting introduces large errors[80]. That is because when *f* is low, the signal presented from blood is very low and it approaches zeros even though *b* is not high. This means most of the DWI obtained only contains diffusion information. So a large error is generated by bi-exponential fitting. Pekar et al. introduced a new fitting method called asymptotic fitting to solve this problem[80].

In asymptotic fitting, it is assumed that the second term in Equation 3.1.6 approaches zero when *b* value is high. So *D* is calculated by the mono-exponential fitting of DWI with high *b* values:

$$\boldsymbol{s = s_0 \cdot \exp(-b \cdot D)} \qquad (\mathbf{3.1.7})$$

$$\boldsymbol{s(b) = s(0) \cdot (1 - f) \cdot e^{-b \cdot D} \;=\; s_{int} \cdot e^{-b \cdot D}} \qquad \boldsymbol{(s(0) \cdot f \cdot e^{-b \cdot (D + D^*)} \;\approx 0)} \qquad (\mathbf{3.1.8})$$

where s_{int} is the intersection point of the fitting curve and the *y* axis. The *f* value is calculated by s_{int} and *s(0)* which is the signal intensity of DWI with *b* = 0 *s/mm*^{2}:

$$\boldsymbol{f = 1 - \frac{s_{int}}{s(0)}} \qquad (\mathbf{3.1.9})$$

3.1.3 Apparent diffusion coefficient (*ADC*)

In most biology tissues, diffusion and perfusion exist simultaneously. So instead of *D*, a new parameter called apparent diffusion coefficient (*ADC*) was introduced to

describe the combination effect of both diffusion and perfusion. The relationship between signal intensity and *ADC* is:

$$\boldsymbol{s = s_0 \cdot \exp(-b \cdot ADC)} \qquad (\mathbf{3.1.10})$$

There are two different ways people usually use to calculate *ADC*. The first one is mono-exponential fitting of Equation 3.1.10[78, 79]; and the other one is calculated by Equation 3.1.11[68, 70]

$$\boldsymbol{ADC = \sum_{i=1}^{n} \frac{ln(s_i/s_0)}{b_i}} \qquad (\mathbf{3.1.11})$$

As a parameter including both perfusion and diffusion information, *ADC* is widely applied in tissue character investigation, especially in the study of distinguish malignant tumors from benign tumors and healthy tissue [81, 82].

3.2 APPLICATION OF DWI IN THERMAL THERAPY OF MRgHIFU OF UTERINE FIBROIDS

In MRgHIFU, after thermal therapy, the NPV should have a higher signal because of the small signal decay caused by low perfusion compared with the non-treated region. As it was mentioned in Chapter 2, many studies described that the application of DWI with a high *b* value as a non-contrast method to monitor the NPV after thermal therapy. In this dissertation we compared the signal relative enhancement between NPV and non-treated region among DWI with different *b* values, and find the best *b* value for DWI to monitor the NPV after thermal therapy.

3.2.1 Method

3.2.1.1 Patient population

Two subjects (42yrs and 45yrs) provided written informed consent to participate in this IRB approved prospective study. HIFU treatment was applied to necrosis the fibroids. The clinical indication for the MR was the imaging evaluation of uterine fibroids before and after thermal therapy. A total of 2 fibroids in the two women were included in the study.

3.2.1.2 Imaging acquisition

All imaging was performed on a commercial 1.5 T MR scanner (Achieva, Philips Medical System, The Netherlands). The patients were positioned supine, and a 16-channel Torso coil was used for signal reception.

<u>CE image</u>

Regular dosage magnevist (0.02 *cc/kg*) was injected before the acquisition. CE image acquisition started 5 min (patient A)/ 6min (patient B) after gadolinium based contrast agent (GBCA) injection. 3D TFE sequence with TFE faction equal to 33 was applied. The flip angle was 10 °. The parameters of the sequence were as following: TE/TR: 2.6 *ms*/5.4 *ms*, Acquired voxel size: 1.49 x 1.89 x 3mm^3, FOV: 250x250 mm^2, Scan time: 2:38*min/slice*.

DWI

DWI was SE single-shot sequence with the following acquisition parameters: TR/TE: 2500 *ms* /68 *ms*; *b*-value: 0, 5, 10, 15, 20, 40, 60, 200, 450, 900 s/mm^2 (patient A)/ 0, 15, 50, 450, 900 s/mm^2 (patient B); parallel imaging acceleration (Sensitivity encoding) factor: 53; half scan factor: 0.717; acquired voxel size: 3 x 3 x 5 mm^3; NSA: 2 (patient A) and 8 (patient B); high-*b* values ($b > 500$ s/mm^2) were averaged (4 (patient A) and16 (patient B)) more than low *b*-values (2 (patient A) and 8 (patient B)); total acquisition time: 02:38 min (patient A) and 05:25 *min* (patient B).

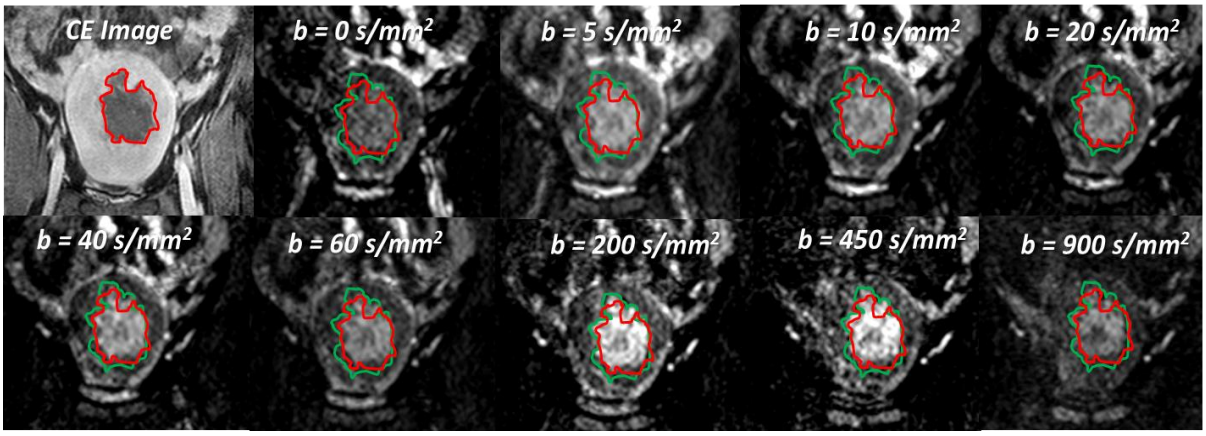

Figure 3-3 *CE image and DWI for patient A after thermal therapy. Coronal views of CE image and DWI with different b values are shown above. The NPV in CE image and DWI are bounded by red and green contour separately.*

3.2.2 Results

CE image and DWI with different *b* values of patient A were shown in Figure 3-3. The dark region in the CE image indicating the NPV was bounded by the red contour, while the bright region in DWI indicating the treated region was circumscribed by a green contour. The NPV measured in CE overlapped with the treated region measured in

DWI quite well. The DICE coefficient ($2 \times (NPV_{CE} \cap DWI\_Volume_{treated\_region})/(NPV_{CE} + DWI\_Volume_{treated\_region})$) was 0.83 for patient A and 0.76 for patient B.

The treated region in the center of the fibroid in DWI was barely distinguished with the surrounding non-treated region when $b = 0$ s/mm^2, which was actually a pure T_2-weighted image. In DWI with $b = 200$ s/mm^2, the treated region appeared much brighter compared with the non-treated region, but the image was noisy. When b value went up to 900 s/mm^2, DWI had low signal intensity and the image quality was poor.

To find out the optimal b value for DWI applied to NPV monitoring, the relative enhancement ($(s_{treated} - s_{non\_treated})/ s_{non\_treated} \times 100\%$) was calculated for all the DWI of both patient A and patient B. The relative enhancements for DWI with same b value of different patients were averaged. The relationship between b value and the relative enhancement is shown in Figure 3-4. It is clear that in DWI with $b = 20$ s/mm^2 and 200 s/mm^2, more enhancement was introduced to the treated region.

3.2.3 Discussion

Published work reported that the DWI with high b value (1000 s/mm^2) can be used to define the treated region after thermal therapy[68, 70]. It was known that the SNR of DWI decreases with the increasing of b value, so it is expected that the low b value DWI may be a better way to monitor the treated region. The primary signal difference between treated region and the non-treated region in DWI after thermal therapy is from the difference of f. As it will be shown in Chapter 3.3.4, f of the treated region approached to

0 (under 10%) while it was high (about 20%) for the non-treated region. As it is shown in Figure3-5, when *f* is fewer than 30%, the signal decay in DWI introduced by *f* is almost

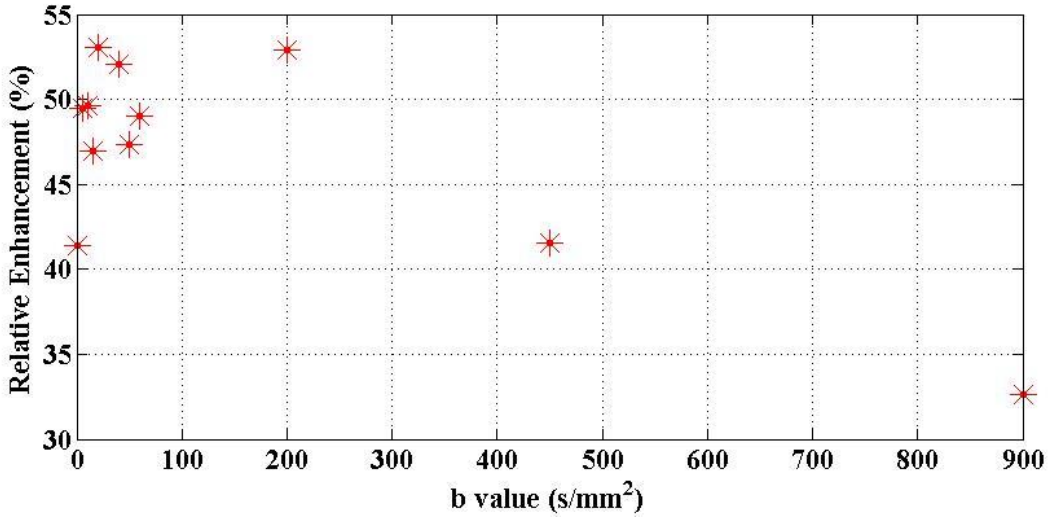

Figure 3-4 *Relationship between relative enhancement of treated region in DWI and b value. The red stars indicate the b value and the corresponding relative enhancement.*

gone when *b* value approaches to 200 *s/mm*^{2} (less than 5% of signal generated by tissue diffusion term), which indicates the contrast of DWI measure with *b* value higher than 200 *s/mm*^{2} mainly introduced by *D*. *f* only affected the contrast of DWI with low *b* value. This is the reason why in the high *b* value DWI, the relative enhancement of the treated region was lower.

Considering both relative enhancement of the treated region and SNR for the whole DWI, *b* = 20 *s/mm*^{2} was a better choice to monitor the treated region after thermal therapy.

Actually, DWI can be not only applied to measure the treated region after treatment, it can also be used during therapy. The scan time for DWI with single *b* value

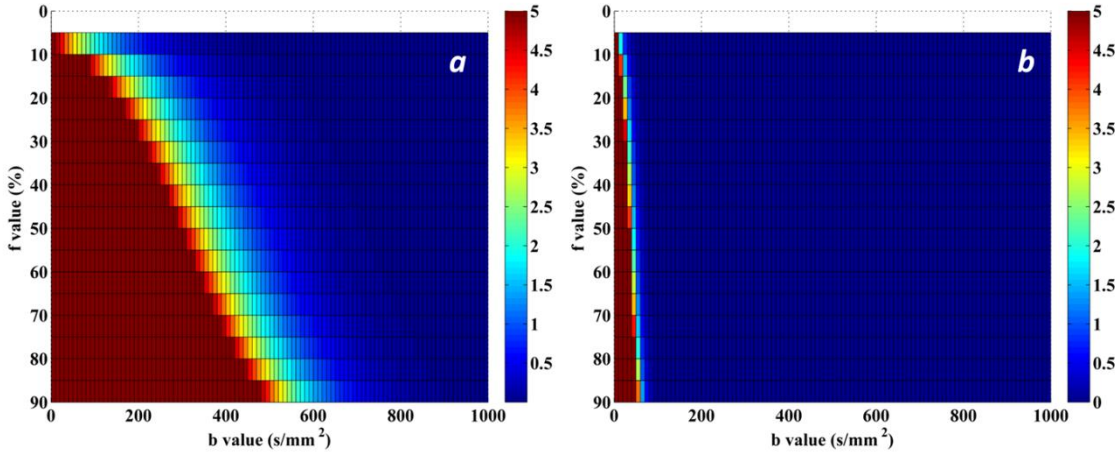

Figure 3-5 *Signal intensity ratio between blood perfusion term and tissue diffusion term. a. D = 0.001 mm^2/s, D* = 0.01 mm^2/s. b. D = 0.001 mm^2/s, D* = 0.1 mm^2/s. The colorbars indicate the signal of blood perfusion term/ signal of tissue diffusion term ×100% (%)*

is very short.

3.2.4 Conclusion

As a non-contrast method, DWI can be used to monitor the treated region both during and after thermal therapy. The treated region measured in DWI overlapped with the NPV in the CE image well. The results from our work suggest that a low *b*-value (20 s/mm^2) DWI generates sufficient diffusion based contrast between the treated and untreated regions, without undue reduction in SNR that is associated with high b-value DWI.

So DWI can be applied as a non-contrast-involved method to estimate the NPV after thermal therapy. The DWI with low *b* value is also a better choice than the ones with high *b* value because of the SNR.

3.3 APPLICATION OF IVIM MODEL IN THERMAL THERAPY OF MRgHIFU OF UTERINE FIBROIDS

As a non-contrast technique, IVIM can be used in tissue microstructure study in MRgHIFU therapy of uterine fibroids. The tissue microstructure can be contributed to make the treatment plan and estimate the treatment results.

3.3.1 Importance of T_2 correction to IVIM model

Reported perfusion information (*f*) of different types of fibroids is similar, which is different with what expected. This may be caused by not considering the different signal decay introduced by the different T_2 between tissue and blood.

3.3.1.1 T_2 correction of bi-exponential fitting of IVIM model

As it is shown in Equation 3.1.6, the first term reflects the signal lose due to tissue diffusion (*D*), and the second term accounts for signal lose due to blood diffusion and perfusion (*D*+*D**), and *f* represents the blood volume fraction per pixel. In the absence of diffusion weighting (*b* = 0 *s/mm*^{2}), MR signal intensity of the tissue and blood compartments are governed by their respective T_2. Therefore, to account for the signal lose at echo time TE in a spin echo experiment, Equation 3.1.6 can be rewritten as:

$$\boldsymbol{s(b) = s_{tissue}(0) \cdot (1 - f_c) \cdot e^{-b \cdot D_c} + s_{blood}(0) \cdot f_c \cdot e^{-b \cdot (D_c + D_c^*)}} \qquad (\mathbf{3.3.1})$$

$$\boldsymbol{s(b) = s_0 \cdot e^{-\frac{TE}{T_2\ tissue}} \cdot (1 - f_c) \cdot e^{-b \cdot D_c} + s_0 \cdot e^{-\frac{TE}{T_2\ blood}} \cdot f_c \cdot e^{-b \cdot (D_c + D_c^*)}} \quad (3.3.2)$$

D_c (D_c*, f_c) is D (D*, f) with T_2 correction.

Studies show that after T_2 correction, f-value decreased compared with the one without T_2 correction [83, 84].

3.3.1.2 T_2 correction of asymptotic fitting of IVIM model

In asymptotic fitting for IVIM model method, T_2 decay also introduces errors. Similar to what we discussed in Chapter 3.3.1.1, T_2 correction of asymptotic fitting is also generated from equation 3.1.6. D and s_{int} are generated by fitting Equation 3.1.8. It is clear that just like bi-exponential fitting, D would not change after T_2 correction, which means T_2 relaxation will not introduce an error in estimation of D. From Equation 3.1.8, we get:

$$\boldsymbol{s_{int} = s_{tissue}(0) \cdot (1 - f_c) = s_0 \cdot e^{-\frac{TE}{T_{2tissue}}} \cdot (1 - f_c)} \quad (3.3.3)$$

Then we get:

$$\boldsymbol{s(0) = s_{int} \cdot \frac{1}{1 - f_c} + s_{int} \cdot \frac{e^{\frac{TE}{T_{2tissue}}}}{1 - f_c} \cdot e^{-\frac{TE}{T_{2blood}}}} \quad (3.3.4)$$

Finally f_c can be obtained by[72]

$$\boldsymbol{f_c = 1 - \frac{s_{int}}{s(0)} \cdot \left(1 + e^{\frac{TE}{T_{2tissue}} - \frac{TE}{T_{2blood}}}\right)} \quad (3.3.5)$$

3.3.2 Application of IVIM model in fibroids classification in MRgHIFU therapy

In this section, we discussed how to applied IVIM model into the investigation of microstructure of different types of uterine fibroids classified by Funaki classification.

3.3.2.1 Method

To evaluate the effect of T_2 correction on the estimation of *f*, the following numerical simulations were performed. T_2 of blood was assumed to be 290 *ms* at 1.5T from published results[85], and all simulations were done in MATLAB™.

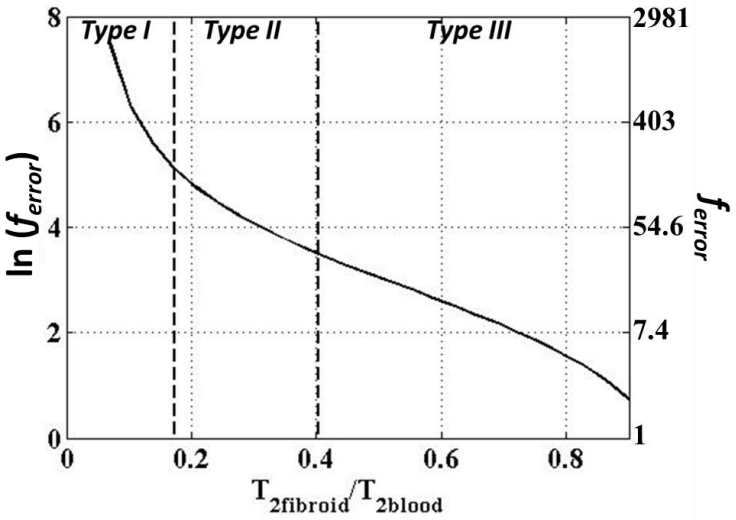

Figure 3-6 *The effect of T_2 correction on blood volume fraction estimation. Note that the estimation of blood volume fraction can be fraught with significant errors without T_2 correction, particularly for Type I fibroids ($T_{2fibroid}$ < 50 ms). The relative error in the estimation of f diminishes when the fibroid T_2 approaches the blood T_2 (Type III fibroids), but still substantial. The dark vertical dotted lines indicate typical T_2 cut off values between Type I and II, Type II and III fibroids.*

Numerical simulation of relationship between T_2 and f_{error} without T_2 correction

To model the large variations in the T_2 of uterine fibroid tissue, a range of T_2 values of fibroid tissue were considered. The ratios of T_2 of fibroid to blood ranging from 0.07 to 0.85 were used (20 *ms* to 250 *ms* for the T_2 of fibroid). For purposes of simulation, slow diffusion component *D* was assumed to be 1×10^{-3} mm^2/s based on previously published reports, and the fast diffusion component *D** was assumed to be about two orders of magnitude greater, i.e., $0.1 mm^2/s$. Blood volume fraction with (f_c) and without (f) T_2 correction was calculated, and f_{error} ($(f-f_c)/f_c*100$) as a function of T_2 ratio was also calculated (Figure 3-6).

MRI data acquisition

All imaging was performed on a commercial 1.5 T MR scanner (Achieva, Philips Medical System, The Netherlands). The patients were positioned supine, and a 16-channel Torso coil was used for signal reception. The imaging protocol consisted of initial scout imaging, and a 3-dimensional T_2-weighted anatomic imaging to localize of uterine fibroids within the pelvic cavity. This was followed by a spin echo single shot, diffusion weighted MR imaging sequence with the following acquisition parameters: TR/TE: 2500 *ms* /74 *ms*; *b*-value: 0, 20, 40, 60, 100, 200, 400, 600, 800, 1000 s/mm^2; parallel imaging acceleration (Sensitivity encoding) factor: 53; half scan factor: 0.717; acquired voxel size: 3 x 3 x 5 mm^3; NSA: 4; high-*b* values ($b > 500$ s/mm^2) were averaged (8 NSA, 12 NSA for 1000s/mm^2) more than low *b*-values (4 NSA); total acquisition time: 06:42 *min*. After DWI, a T_2 map of the uterine fibroid of interest was evaluated in three

orthogonal planes by using a multi-echo turbo spin echo (TSE) sequence with the following acquisition parameters: TR/TE/ΔTE: 2000 *ms*/12 *ms*/12 *ms*; number of echoes: 12; acquired voxel size: $3 \times 3 \times 5\ mm^3$; acquisition time: 06: 42 *min*.

Data Analysis

Calculation of T_2 maps

The images were exported to a vendor specific image format (PAR/REC) and were analyzed on a personal computer by using custom written software in MATLAB™. The T_2 of the uterine fibroid was calculated by fitting the multi-echo data to a single exponential decay curve using a non-linear least square algorithm on a pixel by pixel basis.

Calculation of IVIM model parameters

The multi-*b* value signal decay curve was fitted to Equation 3.1.6 to obtain uncorrected IVIM model parameters *D*, *D**, and *f*. The same data were then fitted to Equation 3.3.2, by using the pixelwise T_2 values estimated previously, to obtain D_c, D_c*, and f_c. Only those pixels which could be fitted with a goodness of fit (R-squared) statistic ($gof_{R\text{-}square}$) > 0.9 were used in the analysis. Pixelwise *ADC* values were also calculated from DW images obtained with *b* values 0, and 1000 mm^2/s.

The correlation between IVIM model parameters and T_2 was assessed by fitting the data to a parametric function that yielded the best fit. *D*-value and *f*-value estimated

with and without T_2 correction were compared using a two-tailed Student's t-test for statistical significance. A $P< 0.05$ was assumed to indicate statistical significance.

3.3.2.2 Results

The T_2 of skeletal muscle in 9 subjects was 42.5 +/- 5.5ms. Fibroids with T_2 values less than 48 *ms* (mean + 1 SD) were classified as Type I fibroids, and fibroids with T_2 values between 48 *ms* and 130 *ms* (T_2 of myometrium) were classified as Type II fibroids. The T_2 values of the 18 uterine fibroids included in the study spanned a large range from 41 *ms* to 95 *ms*. There was substantial heterogeneity of T_2 values in some fibroids.

Of the 18 fibroids evaluated, 6 fibroids were classified as Type I fibroids (mean: 44.39 +/- 1.20 *ms*; range: 42.46 to 45.95 *ms*). Twelve fibroids (mean: 61.90+/- 12.9 *ms*; range: 51.56 to 94.91 *ms*) were classified as Type II fibroids. No Type III fibroids were observed in this study.

<u>IVIM Model Parameters:</u>

A representative DWI of the uterine fibroid acquired with various '*b*' values is shown in Figure 3-7. The color-coded *f* map and f_c map are also shown in figure panel (far right). Note that f_c is substantially smaller than *f*.

A summary of IVIM model parameters estimated with and without T_2 correction is shown in Table 1 along with the calculated *ADC* values. As predicted by theory, T_2 correction did not substantially alter *D* or *D** -value, but had a substantial influence on *f*-value (Table 3-1, Figure 3-8). Independent of the fibroid type, f_c was significantly

smaller than *f*. Furthermore, after T_2 correction, f_c of Type II fibroids was significantly higher than that of Type I fibroids (*P* <0.05, Table 3-1).

It is worth noting that IVIM model descriptors *D*, *D**, *f*, and *ADC* of Type II fibroids were slightly elevated in comparison to Type I fibroids. However, this elevation did not rise to the level of statistical significance (*P* = NS, Table 3-1).

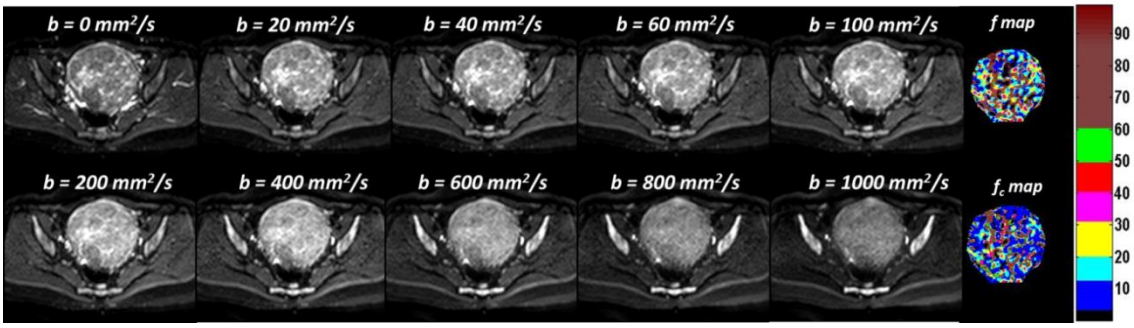

Figure 3-7 *DW images of a heterogeneous uterine fibroid (T_2 value: 69.32 +/- 18.39 ms) is shown above. The color-coded f map and f_c map are also shown (far left). Note that the f_c is substantially lower than f. Colorbar indicates the value of f and f_c (%).*

3.3.2.3 Discussion

In this regard, IVIM-based tissue characterization may be particularly advantageous in that it provides quantitative information about both local tissue microstructure as well as local perfusion. Wang et al. used the IVIM model to evaluate uterine fibroid tissue in terms of *D*, *D**, *f*, and *ADC*. Inkink et al. also used IVIM model to evaluate *D* and *f*. They both reported that, while *D* values of fibroids increased as a function of Funaki classification (from Type I through Type III), there was no statistically significant increase in *f*. Wang et al. also found that *ADC* value increased as a Funaki classification while *D** did not. Although both of these works did not report the T_2 of

uterine fibroids, their results suggest there is a relationship between D and T_2, and the IVIM model used by Wang and Inkink did not take into account the potential error introduced by the T_2 difference between the fibroid tissue and blood. In this dissertation, we sought to assess the influence of T_2 correction on the estimation of IVIM model parameters to characterize uterine fibroid tissue.

Table 3-1 Summary of IVIM parameters and *ADC* of fibroids classified as Type I or II based on T_2 maps.

IVIM-DWI Parameter	D ($\times 10^{-3}$ mm^2/s)	D_c ($\times 10^{-3}$ mm^2/s)	D^* ($\times 10^{-3}$ mm^2/s)	D^*_c ($\times 10^{-3}$ mm^2/s)	f (%)	f_c (%)	ADC ($\times 10^{-3}$ mm^2/s)
Type I	0.75±0.14	0.75±0.13	112.97±77.59	120.03±73.71	24.93±3.94	10.58±2.60	0.96±0.13
	P = 0.5995		P = 0.4437		P = 3.49E-05		
Type II	0.81±0.19	0.82±0.20	132.93±128.53	135.02±130.16	28.00±3.85*	15.89±4.93	1.08±0.23
	P = 0.1102		P = 0.4304		P = 1.26E-09		
Type I vs. Type II	P = 0.5038	P = 0.4396	P = 0.8512	P = 0.7986	P = 0.1321	P = 0.0264	P = 0.2421

First, the results from the study confirm the theoretical predictions (Figure 3-9) that the blood volume fraction (f) of uterine fibroids estimated without T_2 correction can have unacceptably large errors (Figure 3-5). For example, f_{error} of Type I fibroids can range from 50% to 200% of the true value, rendering their estimation clinically moot. Without T_2 correction, the f-values calculated in this study were no different across fibroid types, and this result is similar to what has been reported. After T_2 correction, f_c of Type II fibroids (15.89±4.93%) was significantly higher than Type I fibroids (10.58±2.60%), and this difference was statistically significant (P<0.05), suggesting that

corrected blood volume fraction, f_c, could be a quantitative biomarker of uterine fibroid tissue. Although none of the fibroids evaluated in this study were of Type III, it is worth noting that the high signal intensity of Type III fibroids implies a longer T_2 for these fibroids, compared to Type I and II fibroids. Therefore, the impact of T_2 correction on the estimation of blood volume fraction of Type III fibroids will be substantially lower than that of Type I or II fibroids.

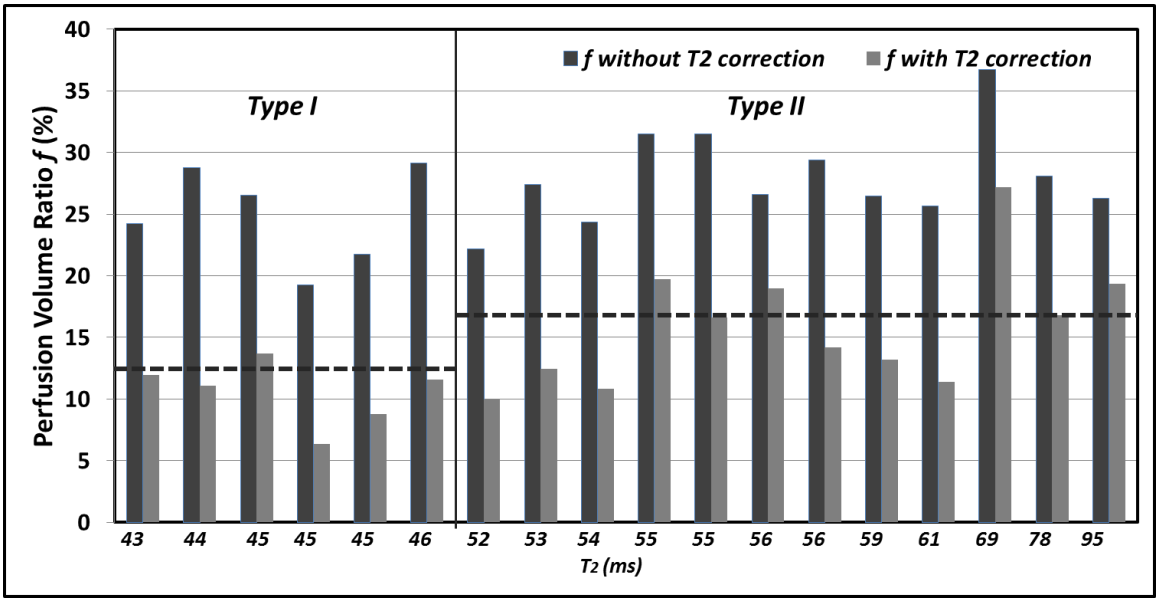

Figure 3-8 *Perfusion volume ratio f and f_c of 18 fibroids included in the study. The black and gray bars represent mean f-value of each fibroid before and after T_2 correction, respectively. The mean value of f_c for Type I and Type II fibroids were marked by dotted lines.*

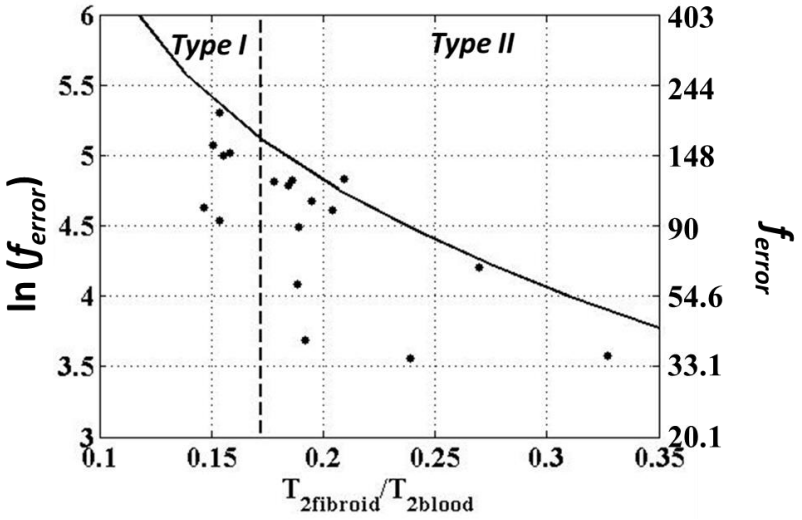

Figure 3-9 *The measured error in the estimation of blood volume fraction (f_{error}) with and without T_2 correction for each of the 18 fibroids is shown above as a function of the T_2 of the fibroid. The theoretically predicted error is shown as a solid line for reference (Figure 1). Notice that the T_2 of blood was assumed to be 290 ms (see text for details).*

We also note that the increase in tissue diffusion and apparent diffusion coefficient (*D* and *ADC*) between Type I and Type II fibroid types could become statistically significant with a larger sample size.

Investigation of relationship between T_2 with *f*, and T_2 with *D*

The Funaki classification indicates that the fibroid with high T_2 value cannot be treated. A recent study also showed the region with high perfusion in the same fibroid required high power to treat. So in this section, we will discuss the relationship between T_2 with *f*, and T_2 with *D* to find out whether the T_2 value related to perfusion or diffusion in the tissue.

3.3.2.4 Methods

Twelve fibroids from experiment in Chapter 3.3.2 were involved in the study.

A histogram of T_2 values from all twelve fibroids was created with each bin spanning a10 *ms* intervals. The mean and standard deviation of the *f*-value and *D*-value (uncorrected and T_2-corrected) of the pixels within each bin was also calculated. Only those pixels that had a $gof_{R\text{-}square} > 0.9$ were included in the analysis. Furthermore, the pixels with *D**-value <*D*-value of free water at 36 ℃ (0.035 mm^2/s) were also excluded, on the assumption that the blood perfusion component should at least be high as the diffusion of free water at body temperature.

3.3.2.5 Results

As the T_2 of the fibroid increased, there was a corresponding increase in *D* and D_c, and this increase was non-linear (Figure 3-10), and independent of T_2 correction.

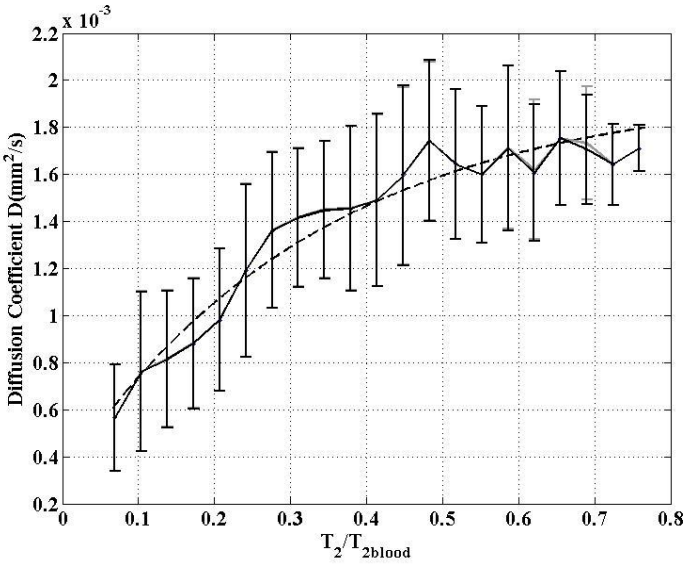

Figure 3-10 *Diffusion coefficient before (gray vertical bars) and after T_2 correction (solid black vertical bars) as a function of fibroid T_2 normalized to blood T_2. The fit (dotted line, Equation 4 in text) indicates that the diffusion coefficient asymptotically reaches the blood diffusion coefficient, and T_2 correction has negligible effect in the measurement of diffusion*

The relationship between T_2 and D_c can be fitted well with a simple exponential function of the form shown below ($gof_{R\text{-}square} = 0.95$):

$$\boldsymbol{D_c(T_2) = -1.66 \times 10^{-3} \cdot e^{-2.98\frac{T_2}{290}} + 1.97 \times 10^{-3}} \quad (\mathbf{3.3.6})$$

It is worth noting that D_c asymptotically approaches 1.9×10^{-3} mm^2/s, as the T_2 of the tissue of interest exceeds the T_2 value of blood (290 *ms*).

In contrast, there was no discernible relationship between *f* and T_2. However, f_c values increased monotonically with increasing T_2 (Figure 3-11), and could be well fitted with a function of the form described below ($gof_{R\text{-}square}$= 0.93):

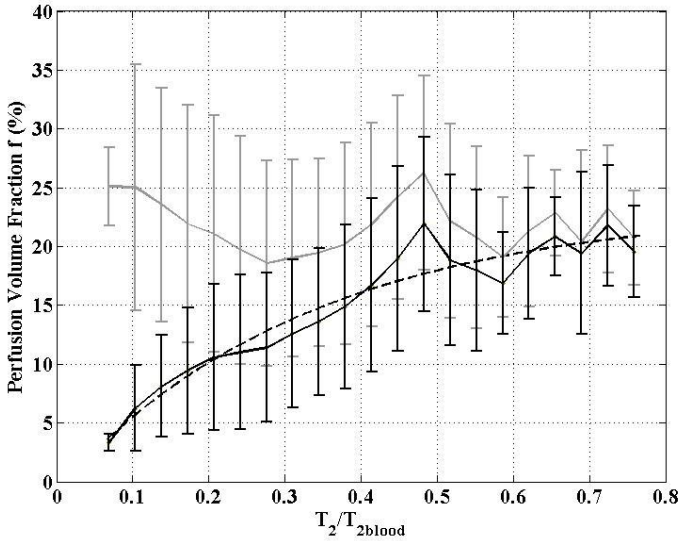

Figure 3-11 *Perfusion volume fraction (f, gray vertical bars) and after T_2 correction (f_c, solid black vertical bars) as a function of fibroid T_2 normalized to blood T_2. The fit (dotted line, Equation 5 in text) indicates that with T_2 correction, f_c increases monotonically to a plateau, as T_2 of fibroid approaches T_2 of blood.*

$$f_c(T_2) = -0.2408 \cdot e^{-3.002\frac{T_2}{290}} + 0.2333 \qquad (3.3.7)$$

Note that f_c asymptotically approaches a blood volume fraction value of 22.13%.

3.3.2.6 Discussion

As predicted by theory, the results from the study show that the estimation of *D* or *D** are not affected by T_2 correction. It is worth noting, however that, diffusion coefficient *D* increases monotonically with increasing T_2 (Figure 4-8) to a plateau of

about 1.9×10^{-3} mm^2/s – a value less than that of free water diffusion at body temperature, presumably due to the protein and cellular content of blood. We note in passing that *D* measured within small regions of blood vessels were close to this asymptotic limit, and this observation has to be confirmed in more careful studies.

3.3.3 Tissue microstructure investigation after HIFU therapy of uterine fibroids

After thermal therapy, the microstructure of the NPV changes. The results reported in Chapter 3.2 only show that the treated region was non-perfused, which is already known, but no details of the microstructure variation were included. In this section, we investigated the microstructure change of NPV after thermal therapy by the IVIM model, which includes both perfusion and diffusion information.

3.3.3.1 Method

All the data were from the same experiment mentioned in Chapter 3.3.2.1.

For both patient A and patient B, pixselwise *D* maps were calculated by asymptotic fitting from high *b* value DWI (*b* = 200, 450, 900 s/mm^2) by (Equation 3.1.8). *ADC* maps were calculated from DWI obtained with *b* values 0, and 900 s/mm^2.

For patient A, an *f* map without T_2 correction (Equation 4.1.9) and with T_2 correction (Equation 3.3.4) was calculated. Mean T_2 value for the non-treated region (60 *ms*) and the treated region (69 *ms*), both calculated by the T_2 map, were applied to T_2 correction IVIM model calculated. A thermal dose volume (TDV) map was generated from temperature evolution during heating.

3.3.3.2 Results

T_2 map of fibroid after thermal therapy

The T_2 map of the whole fibroid after thermal therapy is shown in Figure 3-12.

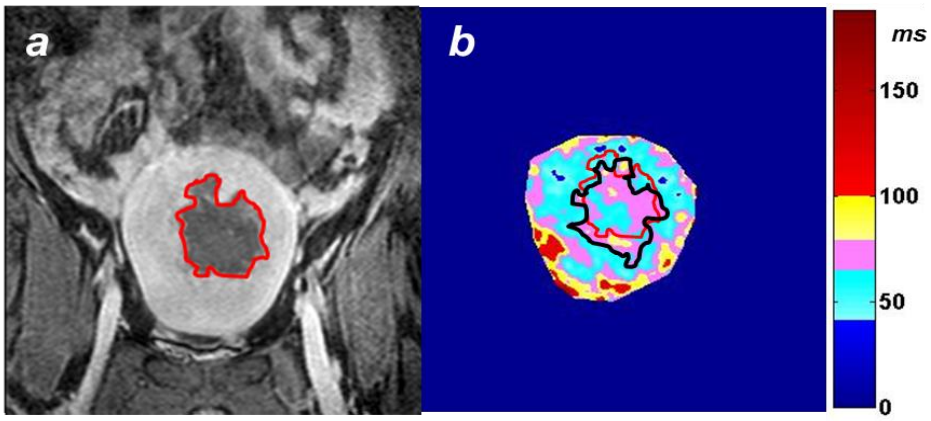

Figure 3-12 *T_2 map of the fibroid after treatment compared with the CE. a. Coronal view of CE image of uterine fibroid after treatment. b. T_2 map of uterine fibroid of the same slice and same view. NPV in CE image was surrounded by red contour. High T_2 value region in T_2 map was surrounded by black contour. Colorbar indicates the value of T_2 (ms).*

It shows clearly that the NPV in CE image overlapped with the region with high T_2 value in T_2 map. DICE coefficient was 0.72 which a little big lower than the DICE coefficient between NPV in CE image and DWI. The mean T_2 value was 59.9 *ms* for the non-treated region and 68.9 *ms* for the treated region. In the T_2 map shown in Figure 3-13, some pixels in the treated region had low T_2 value, while some pixels in the non-treated region had high T_2 value.

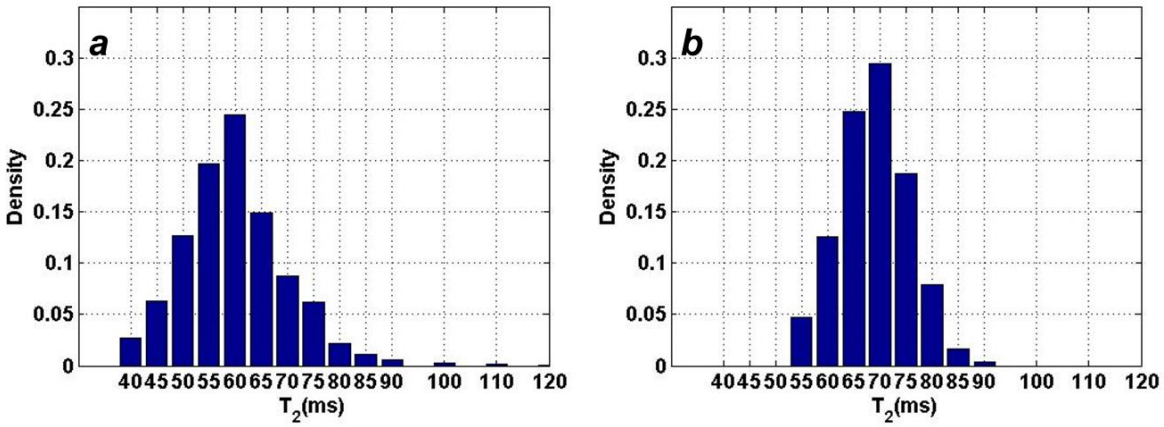

Figure 3-13 *Histogram of T_2 value for treated and non-treated region. a. T_2 value histogram of non-treated region. b. T_2 value histogram of treated region.*

Figure 3-11 shows the T_2 histogram for both treated and untreated region. In the non-treated region, 80% of the pixels had T_2 values less than 65 *ms*, while in the treated region, 65% of the pixels had T_2 values larger than 65 *ms*.

f–value map with and without T_2 correction

The *f* map and the f_c map are shown in Figure 3-14. The f_c map had a lower value than the *f* map. The center of both *f* map and f_c map had lower value than the surrounding region. DICE coefficient between NPV in CE image and *f*-value was high (0.81). However, there were still 30% pixels in the treated region that had high *f* values (>10%). As reported by Bihan et al.[86], tissue perfusion is determined by both *f* and *D**. We compared the TDV with the *f* map and the f_c map combined with *D** map (Figure 3-15).

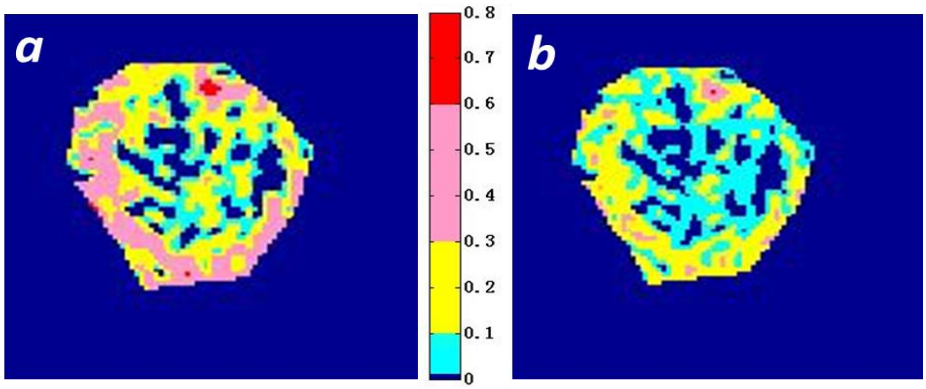

Figure 3-14 *f map and f_c map of uterine fibroid. a. f map (without T_2 correction). b. f_c map (with T_2 correction). Colorbar indicates the value of f and f_c.*

In Figure3-15a, the TDV overlapped on the brighter region indicating NPV in DWI. We assumed the voxels with *f*-value >10% and $D^* > 0.001$ mm^2/s had high perfusion. Only the mauve voxels in Figure 3-15b had high perfusion. No high perfusion voxels were found in Figure 3-15c. So without T_2 correction, 29% voxels with high TD (> 240 EM) had high perfusion, but with T_2 correction, all voxels with high TD (>240 EM) had low perfusion.

<u>*D* map and *ADC* map</u>

The *D* map and *ADC* map for both patient A and patient B are shown in Figure 3-16. No difference between is seen treated and non-treated region in *ADC* map for either patient A or patient B. The treated region and the region surrounding had a higher *D* value compared with the non-treated region. However, it was hard to identify the treated region from the *D* map.

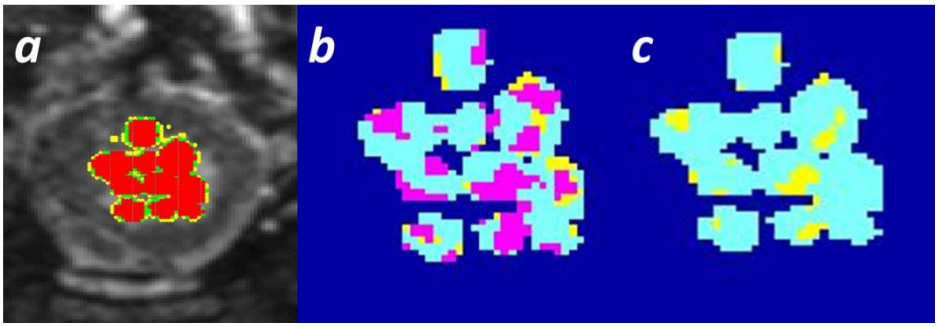

Figure 3-15 *TDV map compared with f map and f_c map combined with D*. a. TDV overlapped with DWI (b = 60 s/mm^2). Red dots (TD >240 EM). Green dots (100 EM<TD<240 EM). Yellow dots (30 EM<TD<100 EM). b. f map combined with D* for all the voxels with TD >240 EM. c. f_c map combined with D* for all the voxels with TD >240 EM. Teal: f-value <10%. Mauve: f-value >10% and D* >0.001 mm^2/s. Yellow: f-value >10% and D* <0.001 mm^2/s.*

3.3.3.3 Discussion

After thermal therapy, the treated region had higher T_2 values compared with the surrounding non-treated region. This may be caused by the edema formed after the tissue was destroyed. The high DICE coefficient between the NPV in CE image and the high T_2 value region in the T_2 map, indicated the T_2 map can be used as a tool to estimate the treatment result without contrast after treatment.

The previous studies reported that the TDV (>240 EM) overlapped with NPV in CE image very well, which means all voxels with TD > 240 EM are non-perfused. The non-perfused may be caused by the contraction or blockage of the blood voxel, which can be indicated by *f-value*, or caused by very slow blood flowing, which can be indicated by *D**. Without the T_2 correction, 29% of TDV (>240 EM) still had high perfusion. But after the T_2 correction, most voxels of TDV (>240 EM) had very small f_c which means the blood vessels were destroyed. Very few voxels had high f_c and low *D**, which indicates

the blood vessels inside these voxels were not destroyed. However, the blood supply from other region decreased, and the blood flowing was slow. So, T_2 corrected is necessary when using IVIM model to investigate the tissue microstructure change after thermal therapy.

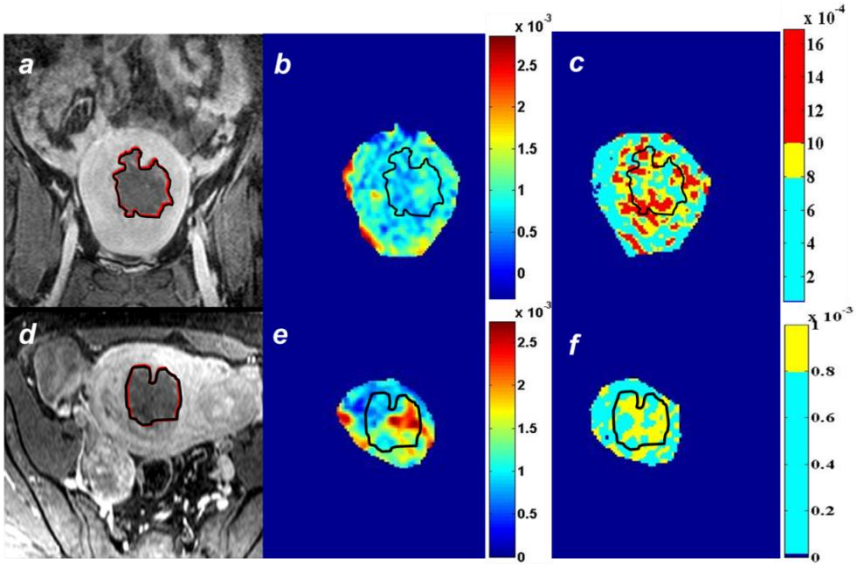

Figure 3-16 *D map and ADC map compared with CE image for both patient A and patient B. Patient A (a-c): a. the coronal view of CE image of fibroid. b. ADC map of fibroid. c. D map of fibroid. Patient B (d-f): d. the coronal view of CE image of fibroid. e. ADC map of fibroid. f. D map of fibroid. The NPV in CE image was surrounded by black contour. Colorbars indicate D or ADC value (mm^2/s).*

Right after thermal therapy, there are some pixels with very low f_c (under 5%) but very high D^* (about $0.1mm^2/s$). As it was reported by Change et al., instead of bi-exponential fitting, asymptotic fitting generates results with lower errors. So, asymptotic fitting was applied in IVIM model calculation for the fibroids right after treatment. *ADC* showed no difference between treated and non-treated region, but *D*-value increased after

tissue necrosis. The other published papers that discussed *ADC* maps of uterine fibroids reported that *ADC* for the treated region was higher than non-treated region[68-71]. The difference results were caused by the difference ways to calculate *ADC* value. In the published work[68-71], *ADC* was calculated by Equation 3.1.11, so *ADC* included all the perfusion and diffusion information (including *f*, *D*, and *D**). However, in this dissertation, *ADC* was calculated by,

$$\boldsymbol{ADC = \frac{ln(s(b_1) - s(b_2)}{b_1 - b_2}} \qquad (\mathbf{3.3.8})$$

As it was reported by Bihan et al.[73], when $b_1 = 0$, b_2 is high and f is low,

$$\boldsymbol{ADC \approx D + \frac{f}{b_2}} \qquad (\mathbf{3.3.9})$$

The treated region had 10% to 20% lower *f*-value (Figure 4-14) than the non-treated region, so the difference of *ADC* introduced by *f* was less than $0.2 \times 10^{-3} mm^2/s$. And this small decrease of *ADC* was compensated by the increase of *ADC* introduced by *D*. This was the reason why in results reported in this dissertation, no *ADC* difference was shown between treated and non-treated region.

3.3.4 Tissue microstructure investigation for the treatment following up of uterine fibroids

3.3.4.1 Method

Patient population

Patient A came back 12 months after treatment. The clinical indication for the MR was the imaging evaluation of uterine fibroid.

MRI acquisitions

DWI with 7 *b* value were obtained (*b* = 0, 50, 100, 200, 400, 600, 800, 1000 *s/mm*^{2}). TR/TE: 2500ms/ 71ms. Scan time: 8:33min. NSA: 18, high-*b* values (*b* > 500 *s/mm*^{2}) were averaged (36 NSA, 54 NSA for 1000*s/mm*^{2}) more than low *b*-values (18 NSA). The other parameters were the same with DWI acquisition in Chapter 3.3.1. T_2 measurement and CE image were measured by the same sequences and parameters used in Chapter 3.3.1.

Data analysis

Pixselwise T_2 map was calculated. Bi-exponential fitting of IVIM model with and without T_2 correction was applied to generate *f* and f_c map.

3.3.4.2 Results

The mean value of T_2 for the NPV was decreased to 38 *ms*. CE image, *f*, and f_c maps are shown in Figure 3-15.

After 12 month, the whole fibroid was necrosis (Figure 3-17a). A clear edge between NPV and myometrium was shown in f_c map (Figure 3-17c). The treated region had a lower *f*-value (most of the voxels had *f* <10%), while the myometrium had a higher *f*-value (>10%). But in the *f* map, it was hard to distinguish the treated region and myometrium (Figure 3-17 b).

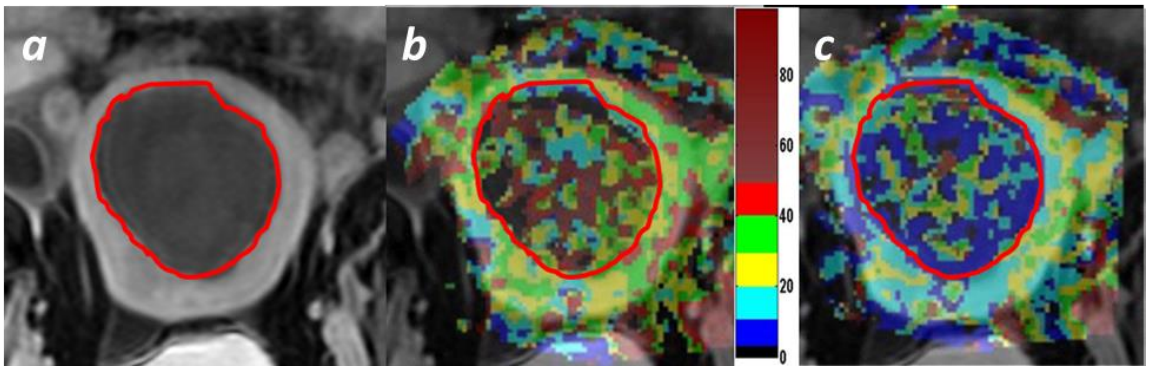

Figure 3-17 *CE image, f map, and f_c map of fibroid in the 12 months following up study. a. A uterine fibroid treated with MRgHIFU shows the characteristic lack of enhancement in a post-contrast MR scan at the 12 month follow-up (region bounded by the red contour). The bright region surrounding the non-perfused volume (circumscribed by a red contour) is the enhancing myometrium. Blood volume fraction maps before (b) and after (c) T_2 correction are overlaid on post-contrast MR scan. Notice the substantial reduction in f_c (panel C) compared to f (panel B). Colorbar indicates the value of f and f_c (%).*

3.3.4.3 Discussion

With the IVIM model-based diffusion analysis, T_2-corrected blood volume fraction (f_c) can serve as a perfusion-related parameter that provides equivalent information as NPV, without using contrast. The potential application of f_c maps as a non-contrast biomarker to monitor MRgHIFU treatment response needs to be explored further.

3.3.5 Conclusion

IVIM model can be used in the investigation of tissue microstructure, including tissue diffusion and perfusion in MRgHIFU therapy of uterine fibroids. It is worth noticing that the T_2 of fibroids tissue is much smaller than the T_2 of blood, which introduces a large error without applying the T_2 correction in IVIM model analysis for both bi-exponential fitting and asymptotic fitting. The *f*-value was different for different

types of fibroids classified by the Funaki classification only when the T_2 correction was taking account. Type II fibroids had significantly low f_c compared with Type I fibroids. *f*, *D*, *D**, and *ADC* did not show significant difference (P>0.05).

The f_c value may be a new way to classify uterine fibroids. Besides, the f_c map can be used as a non-contrast method of treatment result estimation. Right after treatment, the treated region had a higher T_2 value but lower *f* and f_c value. No significant change in *ADC* but an increase in *D* was observed. However, from the *D* map, it was hard to identify the treated region. Compared with the *f* map, the f_c map was much better correlated to TDV (>240EM). Twelve months after therapy, the T_2 of the treated region had decreased. There was a clear boundary between the treated and non-treated region, and the treated region had a lower f_c-value. So only the f_c map can be applied as a non-contrast agent involved method to estimate the treatment result both after treatment and in the following up study.

So, T_2 correction is required in the application of IVIM model in microstructure investigation of uterine fibroid in MRgHIFU therapy. Non-treatable fibroids have higher *f*-values, which indicates the higher blood perfusion may be one of the reasons introducing difficulties to the treatment. The f_c and T_2 maps can be applied as a tool to estimate non-contrast involved treatment results, which can be benefit to the patients with a dysfunctional kidney.

4 MODIFICATION OF T_2-WEIGHTED IMAGING IN MRgHIFU THERAPY OF UTERINE FIBROIDS

As it was discussed in Chapter 2, the long pre-treatment scan time may cause many problems, including introducing blood vessel ablation and making patients uncomfortable. It can also reduce the real treatment time (sonication time) so that the treatment efficiency is reduced.

Because of high SAR, low SNR, and low spatial resolution, the scan time cannot be reduced by a conventional TSE sequence with a very high TSE factor. In this chapter, we introduced a modified TSE sequence which combines ZOOM and variable refocusing flip angles with conventional TSE sequence to reduce scan time. Simulation and clinical human experiment results are also reported.

4.1 THEORY

The modified multi-shot TSE sequence reduces acquisition time by (1) reducing phase encoding by ZOOM technique and (2) increasing the TSE factor by applying variable refocusing angles to keep the image quality and reduce SAR.

4.1.1 ZOOM technique

Buecker et al. introduced a new technique to reduce the scan time which is called the ZOOM technique in 1998[87]. The basic idea of ZOOM is to reduce the scan time by reducing the field of view (FOV) of the image. As it is known, when the length of FOV is shorter than the length of the object in phase encoding direction, aliasing will happen.

The part of the body which is outside the FOV in phase encoding direction will be folded over on the image.

To avoid this problem, instead of applying gradient in slice selection direction while applying refocusing angle, that a gradient is applied orthogonally to the slice selection direction (Figure 4-1); and this gradient only makes the spins in the FOV be refocused by the refocusing angles. The spins outside the FOV but inside the imaging slice would not be refocused, so that they would not contribute to generate the image. Then no aliasing happens.

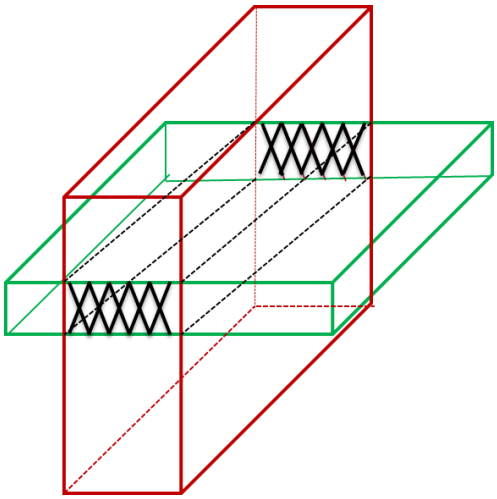

Figure 4-1 *Small FOV excitation by ZOOM technique. The excitation flip angle slice (red) is orthogonal to the refocusing flip angle slice green). So only the protons in the intersection of these two slices are first excited and then refocused, which means only these protons make contribution to the MR image. And this intersection is the required small FOV.*

4.1.2 Variable refocusing flip angles application

To slow down the T_2 decay but not increase SAR, a modification of refocusing angles were applied in TSE sequence with high TSE factor. Instead of keeping all the refocusing angles to be 180°, variable refocusing angles lower than 180° are applied.

4.1.2.1 Variable refocusing angle application

In conventional multi-shot TSE sequence, all the refocusing angles are 180°. Only the M_{xy} is refocused; M_z increases because of T_1 relaxation, but makes no contribution to the signals collected in the same shot. If variable refocusing angles are applied and all of them are smaller than, the situation is much more complex. M_{xy_pre} (M_{xy} before refocusing angle applied) is flipped away from transverse plane and it has both transverse component and longitudinal component. Meanwhile, M_{z_pre} (M_z before refocusing angle applied) is flipped away from longitudinal direction so it also has both transverse component and longitudinal component. Then M_{z_pos} (M_z after refocusing angle applied) used to generate the image signal at TE is contrasted by both M_{xy_pre} and M_{z_pre}[88] (Figure 4-2). This means in the TSE sequence with variable refocusing angles, the image signal intensity will not only be governed by T_2 decay but also by T_1 relaxation during the readout. In this method, the reduction in M_{xy_pre} during the readout due to T_2 decay is partly compensated by the increase in the longitudinal magnetization (M_{z_pre}). This diminishes the rate of signal decay during the readout, thus helping to minimize the loss of spatial resolution due to T_2 decay during the readout.

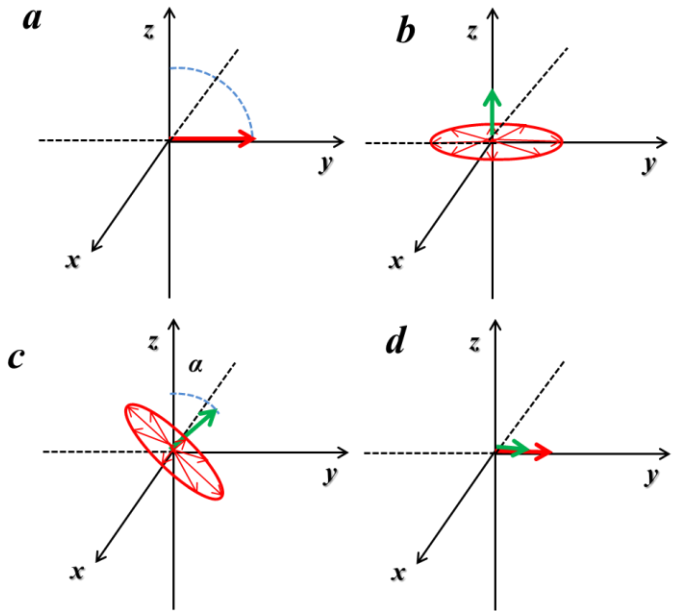

Figure 4-2 *Principle of refocusing by non-180 °refocusing flip angle in SE. a. M_{xy} created after excitation flip angle. b. At TE/2, spins dephasing in the xy plan and M_z introduced by T_1 relaxation. c. At TE/2, after refocusing flip angle α (<180 °) applied. d. New M_{xy} (final signal) at TE. The red component is created by the M_{xy} in b and green component is created by the M_x in b.*

4.1.2.2 Extended phase graph (EPG) algorithm

Unlike the conventional TSE sequence with 180 °refocusing flips, the signal decay cannot be calculated straight forward by the exponential T_2 decay expression in a variable refocusing angles TSE sequence. A method called extended phase graph (EPG) algorithm was introduced to calculated three components of magnetization after a very refocusing angle[89] (Figure4-3).

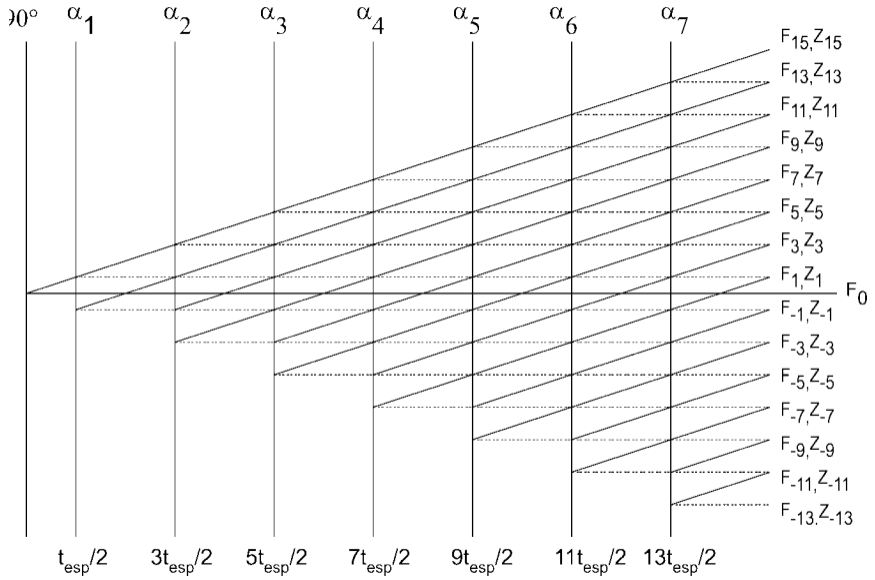

Figure 4-3 *EPG algorithm for TSE sequence with 90° excitation flip angle and α refocusing angles*[89].

$$\boldsymbol{F_n = \int_{\omega-\Delta\omega}^{\omega+\Delta\omega} \left(M_x \cdot \cos(\omega \cdot t_{en}) + M_y \cdot \sin(\omega \cdot t_{en})\right) d\omega} \qquad (\mathbf{4.1.1})$$

$$\boldsymbol{F_n^* = \int_{\omega-\Delta\omega}^{\omega+\Delta\omega} \left(M_x \cdot \cos(\omega \cdot t_{en}) - M_y \cdot \sin(\omega \cdot t_{en})\right) d\omega} \qquad (\mathbf{4.1.2})$$

$$\boldsymbol{Z_n = i \cdot \int_{\omega-\Delta\omega}^{\omega+\Delta\omega} \left(M_x \cdot \cos(\omega \cdot t_{en}) + M_y \cdot \sin(\omega \cdot t_{en})\right) d\omega} \qquad (\mathbf{4.1.3})$$

$$\boldsymbol{Z_n^* = i \cdot \int_{\omega-\Delta\omega}^{\omega+\Delta\omega} \left(M_x \cdot \cos(\omega \cdot t_{en}) - M_y \cdot \sin(\omega \cdot t_{en})\right) d\omega} \qquad (\mathbf{4.1.4})$$

where ω is the magnetization rotation frequency and t_{en} is equal to $n*t_e$, in which t_e is the echo time TE. After the very refocusing angle is applied, *F* and *Z* can be calculated by equation (4.1.5)

$$\begin{bmatrix} F_k^-(n) \\ F_k^{*-}(n) \\ Z_k^-(n) \\ Z_k^{*-}(n) \end{bmatrix} \xrightarrow{rotation\_matrix} \begin{bmatrix} F_k^+(n) \\ F_k^{*+}(n) \\ Z_k^+(n) \\ Z_k^{*+}(n) \end{bmatrix} \xrightarrow{Z_n=-Z_n^*} \begin{bmatrix} F_k^+(n) \\ F_k^{*+}(n) \\ Z_k^+(n) \end{bmatrix} \qquad (4.1.5)$$
$$(k, \alpha_n)$$

$$rotation\_matrix = \begin{pmatrix} \cos^2(\alpha/2) & \sin^2(\alpha/2) & \sin\alpha & 0 \\ \sin^2(\alpha/2) & \cos^2(\alpha/2) & 0 & \sin\alpha \\ \tfrac{1}{2}\sin\alpha & -\tfrac{1}{2}\sin\alpha & \cos\alpha & 0 \\ -\tfrac{1}{2}\sin\alpha & \tfrac{1}{2}\sin\alpha & 0 & \cos\alpha \end{pmatrix} \qquad (4.1.6)$$

where $F_k^-(n)$ is the k^{th} order of F just before the n^{th} refocusing angle is applied and $F_k^+(n)$ is the k^{th} order of F just after the n^{th} refocusing angle is applied. $Z_k^-(n)$ is the k^{th} order of Z just before the n^{th} refocusing angle is applied and $Z_k^+(n)$ is the k^{th} order of Z just after the n^{th} refocusing angle is applied. So it is clear that $F_k^+(n)$ and $Z_k^+(n)$ are equal to $F_k^-(n)$ and $Z_k^-(n)$ multiplied with a rotation matrix, which is only related to the refocusing angle (Equation 4.1.6). After the n^{th} refocusing angle, only $F_0(n)$ will form an echo corresponding to M_{xy} in the Block equation, while $Z_1(n)$ is corresponding to M_z. Figure 4-3, it is clear that both $F_0(n)$ and Z_1 get contributions from all orders of F and Z before this n^{th} flip angle.

Theoretically, refocusing flips can be set to any angles (less than 180°) with any order. However, the angle schedule is very important to the signal profile along phase encoding direction. Sometimes, even a little difference in angle schedules will introduce a huge difference to signal profile. As it is shown in Figure 4-4, there are only 10 out of 80 angles different between angle schedule 1 and schedule 2, but the signal intensity profiles

are very different. Not only the first 10 echoes generated by the first 10 bigger refocusing angles in schedule 1 are higher, but also the rest of the echoes generated by the same flip angles in both schedule 1 and schedule 2 are higher.

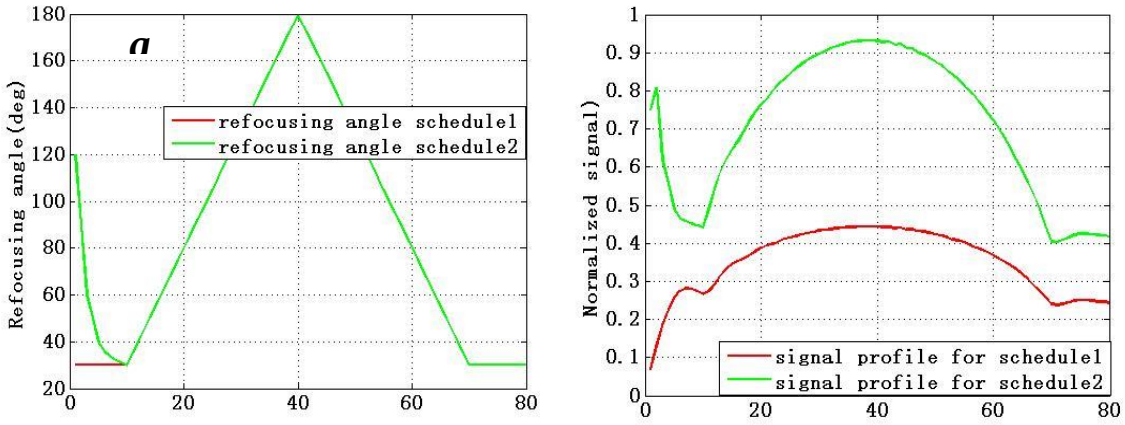

Figure 4-4 *Different refocusing angle schedules and their corresponding signal profiles. a. The refocusing angle schedules. b. The corresponding signal profiles. Red*

So to improve the image quality, the including increasing the SNR and spatial resolution, the design of the refocusing angle schedule is very important.

4.1.2.3 Statistic pseudo steady state

Alsop introduced the definition of statistic pseudo steady state (SPSS) in 1997[90]. It was found that in the TSE sequence with variable refocusing angles, the signal decays most slowly when the system is in SPSS. When system is in SPSS, the three components, including F, F^*, and M_z do not change after every refocusing angles if T_1 relaxation and T_2 decay are not taken into account. Also the M_z-forming echo is calculated by the following equation:

$$M_{echo} = iM_0 exp\left(-i\frac{\beta-\delta}{2}\right)\sin\frac{\alpha}{2}P_{-\frac{1}{2}}\left(\sin\frac{\alpha}{2}\left(1+\frac{\sin^2\alpha}{\sin^4\alpha}\right)\right) \qquad (4.1.7)$$

where M_{echo} is the magnetic resonance component of the echo generated in the SPSS, and α is the last refocusing angle applied before the echo.

The way to force the system to go to SPSS is by applying fast decreasing refocusing angles, starting with a large value (such as 160°or 120°) at the very beginning of refocusing angle schedule. These fast decreasing angles are called startup angles. The signals generated by these refocusing angles are called startup echoes. The system is supposed to reach SPSS after the last starting up angle. The true readout can start after the system reaches the SPSS. It can also including these startup echoes. This depends on the requirement of the image quality. The one with startup echoes has a higher SNR and a shorter scan time, while the one without startup echoes has higher spatial resolution.

4.1.2.4 Refocusing angle schedule design

No combination of fast decreasing angles can force the system to SPSS. Besides, under some situations, there is requirement of the signal intensity (we call it target signal) to be in SPSS. So, the design of the refocusing angle schedule is very important.

Reed Busse et al. introduced the formula for refocusing angle calculation in TSE sequence with any refocusing angle[91],

$$tg\frac{\theta}{2} = \frac{E_1 Z_1 \pm \sqrt{E_1^2 Z_1^2 - (SS - F_1)(SS - F_{-1})}}{SS - F_1} \qquad (4.1.8)$$

$$SS = \frac{S_{target}}{E_2}, \quad E_{1,2} = e^{-\frac{echo\_spacing}{2T_{1,2}}}$$

As shown in Equation (4.1.8), as long as the T_1 and T_2 of the tissue and the target signal are known, the corresponding refocusing angle can be calculated.

4.1.2.5 The limitation of the variable refocusing angles method

As we discussed above, the variable refocusing angles method is very powerful, but it has its own limitations.

The first limitation is the target signal cannot be set to any just value. Because T_2 decay always exist and is much faster than T_1 relaxation, if the target signal is set too high, it will never be achieved. Under this situation, the square root term in Equation (4.1.8) will not generate a real value, which makes the right side of the equation meaningless and the corresponding refocusing angle does not exist.

The second limitation is that the motion effect is significant if the target signal filled in the center of *k-space* is too low. Madhuranthakam et al. reported that the motion effect will be introduced the signal decay if target the signal was too low[92].

Besides, because the echo signal is affected by both T_1 and T_2, the contrast generated in variable refocusing angles TSE image is determined by the refocusing angle schedule. Because the angle schedule is designed using the T_1 and T_2 of only one tissue (we call it target tissue), the signal profiles of the other tissues behave in an

uncontrollable way. This introduces significant problems in generating the contrast between target tissue and the other tissues.

So, in the variable refocusing angle method application, not only are SNR and spatial resolution the primary factors required to be considered, the limitation of the target signal, the motion effect, and the signal intensity behavior of other tissues are also important.

4.2 METHODS

In this study, we introduced a modified TSE sequence combing ZOOM technique and variable refocusing angles method together, to reduce the scan time and increase the SNR and CNR.

4.2.1 Sequence design

4.2.1.1 Target tissue selection

Depend on the size of the fibroids, the ZOOM technique supplied different scan time reduction factor. Because the T_2 of uterine fibroids has a large range (from under 50 *ms* to more than 130 *ms*), unless it is measured before the refocusing angle schedule design, the fibroid cannot be set as target tissues. Besides, the fibroids with qualified size for HIFU therapy have a relatively large volume (larger than 30*cm* in three dimensions), spatial resolution improvement will not generate benefit for the fibroids image. For all the reasons mentioned above, myometrium is set to be the target tissue. T_2 of myometrium was set to 1390 *ms* based on reported results[85].

4.2.1.2 Refocusing flip angles schedule design

From simulation and experiments results, it was found that the following two conditions were satisfied when TE_{eff} is at 25 *ms*: (1) The motion (breathing) does not affect images quality; and (2) The signal decay of myometrium is slow.

Five refocusing angles were applied before the system reached SPSS. The signal profile for these five echoes was calculated by the following equations:

$$\boldsymbol{S_{target} = e^{-\frac{TE_{eff}}{T_2}}} \qquad (\mathbf{4.2.1})$$

$$\boldsymbol{S_n = 0.5 \cdot \left(1 + S_{target}\right) \quad n = 1} \qquad (\mathbf{4.2.2})$$

$$\boldsymbol{S_n = 0.5 \cdot \left(S_{n-1} + S_{target}\right)} \quad \mathbf{1 <}\ n < 6 \qquad (\mathbf{4.2.3})$$

T_2 is the T_2 value of myometriums. S_n is the signal intensity of the n^{th} echo, and S_{target} is the signal intensity at the first echo when the system achieves SPSS.

After the system reaches SPSS, set the signal profile by the following equation:

$$\boldsymbol{S_n = S_{n-1} \cdot f_{decay_n} \quad n > 5} \qquad (\mathbf{4.2.4})$$

where f_{decay_n} is the signal decay factor varying from 0 to 1 for the n^{th} echo. In the real calculation, f_{decay_n} is first automatically set to 1 and then set to the user input value if S_n is too high to find the corresponding angle. If Sn is still too high, f_{decay_n} is automatically decreased by 1% increments until the corresponding angle is found.

4.2.2 Patient population

One subject with 2 Type II fibroids was included in this study.

4.2.3 MR Sequence

All imaging was performed on a commercial 1.5 T MR scanner (Achieva, Philips Medical System, The Netherlands). The patient was positioned supine, and a 16-channel Torso coil was used for signal reception.

The pulse sequence design coding was done by using Philips Pulse Programming software. Two new parameters TE_{eff} and f_{decay}, were introduced, and are shown on the user interface. TE_{eff} was set to 25ms and f_{decay} was set to 0.96. The startup echo number was set at 5 and all the refocusing flip angles were calculated automatically by the coding.

4.3 RESULTS

The signal profiles of c-TSE sequence and m-TSE are shown in Figure 4-5.

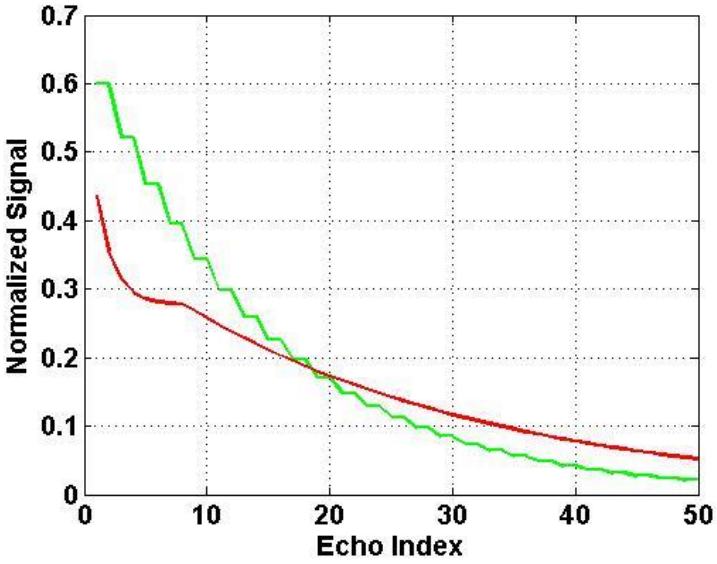

Figure 4-5 *Signal profile of c-TSE sequence and m-TSE sequence. The green line is the signal profile of c-TSE sequence. The red line is the signal profile of m-TSE sequence.*

Both lines shown in Figure 4-5 were signal profiles of myometrium. The signal profile of m-TSE started at a lower value, but it decayed much slower than the signal profile of c-TSE.

Table 4-1 Comparison between c-TSE and m-TSE

Sequence	Shot	Signal Decay	TE (ms)
c-TSE	2 shot/slice	T_2 decay (12%-6%)	130
m-TSE	1 shot/slice	Decay 4%	65

The scan time, signal decay, and TE compared between c-TSE and m-TSE are listed in Table 4-1. The scan time was reduced to half, and both SNR and CNR increased; the CNR between myometrium and fibroid increased from 7% to 9.4%.

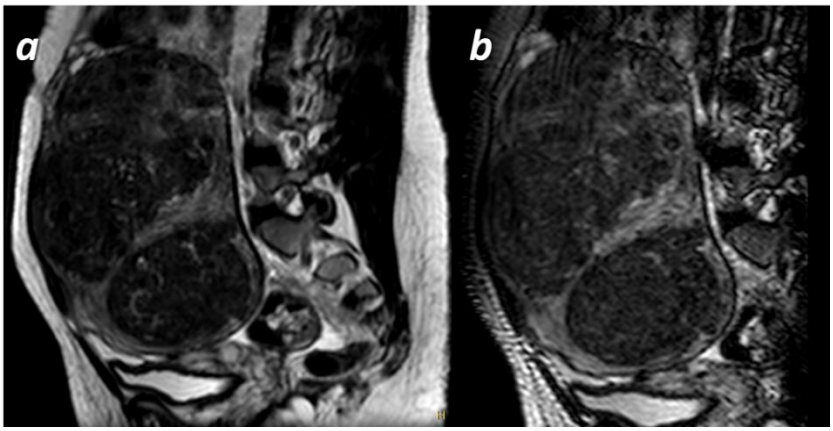

Figure 4-6 *c-TSE and m-TSE images of uterine fibroid. a. Sagittal view of uterine fibroid generated by c-TSE sequence. b. Sagittal view of uterine fibroid generated by m-TSE sequence*

Figure 4-6 shows the images generated in c-TSE and m-TSE sequence of the same fibroid. In the m-TSE sequence, the ZOOM technique decreased the FOV, so the

scan time was reduced. The myometrium appeared much brighter than the fibroid in m-TSE sequence.

4.4 DISCUSSION

In the T_2-weighted image, the c-TSE sequence wastes time because of the large FOV, which includes the back fat and muscle layer. This fat and muscle layer information is useless in the fibroid treatment. The ZOOM technique can reduce the FOV without introducing aliasing.

As it is known, a large TSE factor introduces a high SAR when refocusing angles are high. Besides, the fast T_2 decay in a high TSE factor sequence can cause the low SNR of the image and poor spatial resolution. In the m-TSE sequence, these problems were solved by the application of variable refocusing angles. All the refocusing angles were smaller than 180°. Simulation results showed that when TE_{eff} is 25 *ms,* the target signal is not too high to achieve or too low to introduce large motion effects. Simulation results show only S_6 to S_8 can be set as high as the S_{target}. Several f_{decay} values, including 1, 0.99, 0.98, 0.97, and 0.96 were used in the simulation. The results showed that 0.96 is the value introducing slowest signal decay. The larger f_{decay} factors will make the echo go to too high a value very fast. After the echo signal is too high to reach, f_{decay} automatically drops down very fast.

4.5 CONCLUSION

In this chapter, a modified TSE (m-TSE) sequence was introduced. It was a TSE sequence with ZOOM technique and variable refocusing flip angle application. The

simulation and clinical results show that the scan time of m-TSE was only half of c-TSE, and images generated by the m-TSE sequence had higher SNR and CNR.

By applying m-TSE sequence in the fibroids planning step in MRgHIFU therapy, scan time can be reduced. More time can be used to perform sonication to improve the treatment efficiency. Besides, the m-TSE got rid of the problems that usually happened in high TSE factor TSE sequence, such as high SAR and low SNR, by applying variable refocusing flip angles instead of 180° angles.

The limitation of this study is that only one patient with two fibroids were included, both were Type II fibroids. We have no clinic data to show that Type I and Type III fibroids can also generate good contrast between fibroids and myometrium.

5 TISSUE RESPONSE DURING HEATING

In thermal therapy, diffusion and perfusion of tissue varies during thermal ablation. It reflects the microstructure change caused by the heat. Juan et al. reported that the $ADC_{0\text{-}1000}$ calculated by b = 0, 1000 s/mm^2 increased during heating and decreased during cooling[93]. If the tissue is not damaged, $ADC_{0\text{-}1000}$ goes back to the preheating value, while if the tissue is damaged, $ADC_{0\text{-}1000}$ goes to a lower value when the temperature reduced to body temperature. This phenomenon indicates that $ADC_{0\text{-}1000}$ can be applied as a biomarker of tissue damage. However, people reported that $ADC_{0\text{-}1000}$ of muscle does not have this character[94]. This may be because the muscle tissue has very different perfusion to prostate.

As we discussed in Chapter 3, *ADC* is a combination of diffusion and perfusion information. It is not only determined by the tissue microstructure, but also by the *b* values applied. For example, the *ADC* calculated with 2 low *b* values is more related to the tissue perfusion, while the *ADC* calculated with 2 high *b* values is more related to the tissue diffusion. *ADC* calculated with one low *b* value and one high *b* values is related to both tissue perfusion and diffusion.

In this chapter, we will discuss *ADC* calculated with different combination of *b* values varied during heating, to investigate the microstructure change caused by the heat.

5.1 THEORY

Juan et al. investigated that ADC_{high} ($ADC_{0\text{-}1000}$) of prostate varies with temperature by formula[93]:

$$\boldsymbol{ADC_{high}(T) = ADC_0 \cdot e^{-\frac{E_A}{RT}}} \qquad (\mathbf{5.1.1})$$

in which ADC_0 is a fitting constant which has no physical meaning and does not change with temperature, E_A is activation energy which is the energy required to break hydrogen bonds and does not change with temperature, R is the gas constant, and T is Kelvin temperature. The experimental results show that the experimental $ADC_{0\text{-}1000}$ of non-damage tissue satisfied Equation 5.1.1, while the damage tissue has lower value. However, in another paper, it reported in the other tissue, such as muscle, $ADC_{0\text{-}1000}$ shows no different between damaged and non-damaged tissue[94].

As it was reported, instead of ADC_{high}, D is the parameter whose variation is purely introduced by temperature and follows the formula[95]:

$$\boldsymbol{D(T) = D_0 \cdot e^{-\frac{E_A}{RT}}} \qquad (\mathbf{5.1.2})$$

D_0 is a fitting constant which has no physical meaning and does not change with temperature, and E_A, R, and T has the same physical meaning with Equation 5.1.1. So the Equation 5.1.1 should be written as:

$$\boldsymbol{ADC_{high}(T) = D_0 \cdot e^{-\frac{E_A}{RT}} + f/b} \qquad (\mathbf{5.1.3})$$

To analyze the relationship between ADC_{low} and f, D, and D^*, Taylor expansion was performed on both sides of Equation 5.1.4:

$$\boldsymbol{S_0 \cdot e^{-b \cdot ADC} = S_0 \cdot \left[(1-f) \cdot e^{-b \cdot D} + f \cdot e^{-b(D+D^*)}\right]} \qquad (\mathbf{5.1.4})$$

From the experiment data, $ADC_{0\text{-}20}$ is $<9\times10^{-3}$ mm^2/s and $ADC_{0\text{-}40}$ is $<4\times10^{-3}$ mm^2/s, so only the first two terms of Taylor expansion were taken into account. Then we get:

$$\boldsymbol{S_0 \cdot (1 - b \cdot ADC_{low}) = S_0 \cdot \left[(1 - f) - b \cdot D(1 - f) + f \cdot e^{-b(D+D^*)}\right]} \quad (\mathbf{5.1.5})$$

$$\boldsymbol{ADC_{low} = (1 - f) \cdot D + \frac{f}{b} - \frac{f}{b} \cdot (1 - b \cdot D) \cdot e^{-b \cdot D^*}} \quad (\mathbf{5.1.6})$$

We assume $b \cdot D << 1$ and $f <<1$, then we can get:

$$\boldsymbol{ADC_{low}(T) = D(T) + \frac{f}{b} - \frac{f}{b} \cdot e^{-b \cdot D^*}} \quad (\mathbf{5.1.7})$$

We assumed for each damage region, ADC_0, R, and E_A were the same for both ADC_{low} and ADC_{high}. Then we can get:

$$\boldsymbol{ADC_{low}(T) = ADC_{high}(T) - \frac{f}{b} \cdot e^{-b \cdot D^*}} \quad (\mathbf{5.1.8})$$

So the reason why tissue ADC_{high} showed no different between damage and non-damage region in muscle may be because the change of diffusion compensated the change of perfusion. We separated the whole treatment duration into three periods. The first period starts at the beginning of heating and ends when temperature reaches 48℃. The tissue microstructure does not change and only D varies with temperature (Equation 5.1.3 and Equation 5.1.9).

$$\boldsymbol{ADC_{low}(T) = D_0 \cdot e^{-\frac{E_A}{RT}} + \frac{f}{b} - \frac{f}{b} \cdot e^{-b \cdot D^*}} \quad (\mathbf{5.1.9})$$

The second period is after tissue reaching 48℃ until heating is finished. We assumed the tissue microstructure changes during this period and that the ADC_{high} and ADC_{low} satisfy the following equations,

$$\boldsymbol{ADC_{high}(T) = D_0(T) \cdot e^{-\frac{E_A}{RT}} + f(T)/b} \quad (\mathbf{5.1.10})$$

$$\boldsymbol{ADC_{low}(T) = D_0(T) \cdot e^{-\frac{E_A}{RT}} + \frac{f(T)}{b} + \frac{f(T)}{b} \cdot e^{-b \cdot D^*}} \quad (\mathbf{5.1.11})$$

The third period is the cooling duration. We assumed that tissue blood perfusion is very small and $D_0(T)$ reaches value D_{0max} and does not change in a short amount of time. Then we can get:

$$\boldsymbol{ADC_{high}(T) = D_{0max} \cdot e^{-\frac{E_A}{RT}}} \quad (\mathbf{5.1.12})$$

$$\boldsymbol{ADC_{low}(T) = D_{0max} \cdot e^{-\frac{E_A}{RT}} + f_{min}/b} \quad (\mathbf{5.1.13})$$

5.2 METHOD

5.2.1 MRI Acquisition

A total of 6 treatment cells were performed on two legs of pig (4 on left leg and 2 on right leg). Twenty five watts of HIFU power heated for 8min, and the cooling time was 10 min for each treatment cell. DWI with 4 *b* values (0, 20 (or 40), 350, 450 s/mm^2) and temperature measurements were interpolated during the heating and cooling periods. The acquisition parameters were listed in Table 5-1:

Table 5-1 Sequence parameters in DWI and temperature measurements

	Sequence	TR/TE (ms)	FOV (mm×mm)	Spatial resolution (mm×mm)
DWI	SSH SE-EPI	1500/64	300×300	1.5×1.5×7
Temperature Measurement	GRE-EPI	141/19.5	300×300	1.5×1.5×7

5.2.2 Data Analysis

The TD map was calculated. The region with TD ≥240 EM was the damage region of interest. Mean value of the temperature, ADC_{high} ($ADC_{0\text{-}350}$ obtained by b = 0 and b = 350 s/mm^2) and ADC_{low} ($ADC_{0\text{-}20/40}$ obtained by b = 0 and b = 20 s/mm^2 or 40 s/mm^2) was calculated.

5.2.2.1 ADC_{high} analysis

For each damage region, ADC_0, R, and E_A for ADC_{high} were obtained by fitting all data points during the heating period using Equation 5.1.1. The calculation of ADC_{high} was based on temperature by using Equation 5.1.1 for the whole treatment duration, including both heating and cooling periods.

5.2.2.2 ADC_{low} analysis

Equation 5.1.8 was applied to calculate the difference between ADC_{low} and ADC_{high}, which is related to the perfusion variation with temperature.

5.3 RESULTS

The ADC_{high} of four out of the six treatment cells, both measured and calculated were plotted in Figure 5-1.

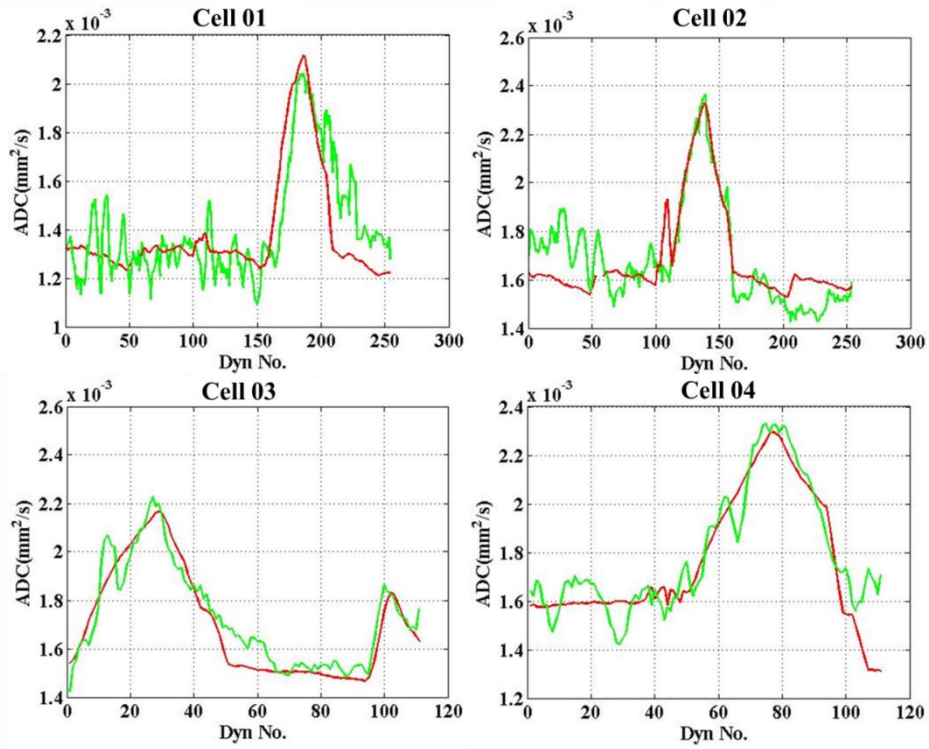

Figure 5-1 *Measured ADC_{high} (green line) and calculated ADC_{high} (red line) for 4 treatment cells. Each dynamic is 23s.*

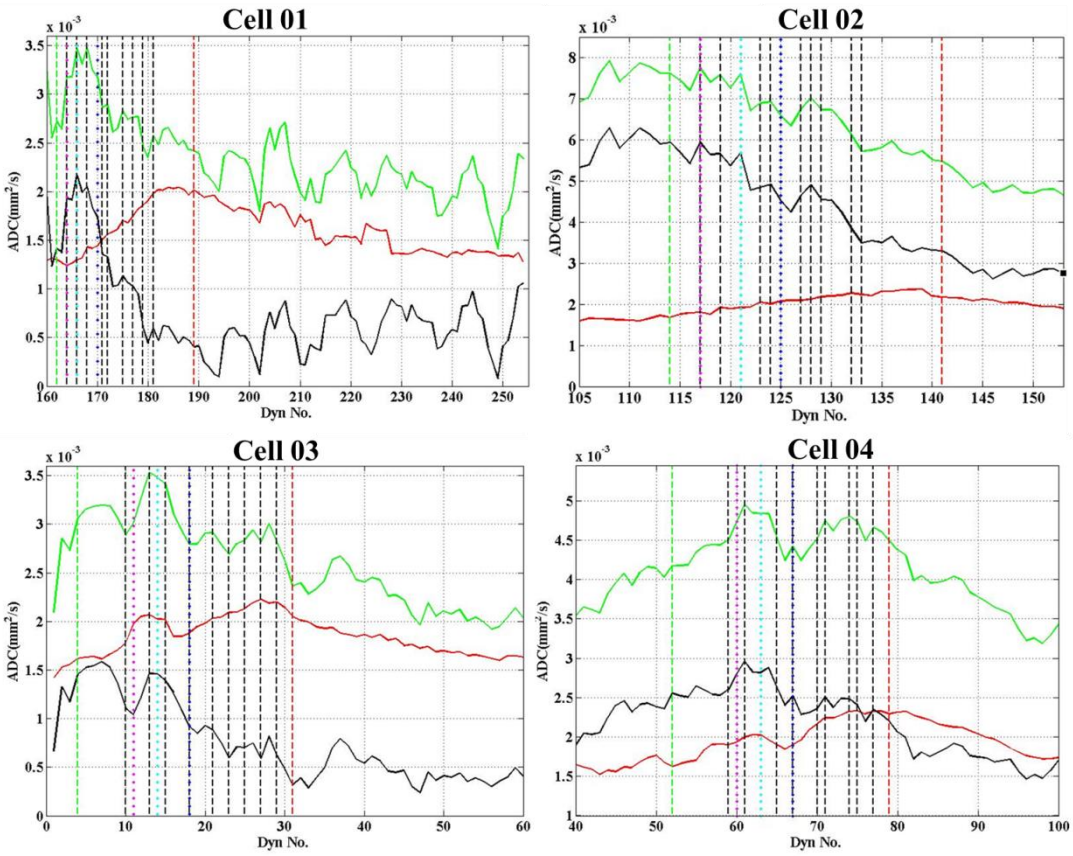

Figure 5-2 *Calculated ADC_{high} (red line), measured ADC_{low} (green line), and the difference between calculated ADC_{high} and ADC_{low} (black line) for 4 treatment cells. Each dynamic is 23s. The green dot lines show the time point starts heating. The red dot lines show the time points end heating. The purple dot lines show the time points the interested region reached temperature 46℃. The baby blue dot lines show the time points the interested region reached temperature 48 ℃. The blue dot lines show the time points the interested region reached temperature 50 ℃. The black dot lines show the time points when x% of the interested region reached TD 240EM (x:10-90)*

Calculated ADC_{high}, ADC_{low} and difference between these two values were plotted in Figure 5-2.

ADC_{high} increased with increasing temperature, and when the temperature went back to body temperature, it decreased to the value before heating. This is the same with the results reported in [94]. ADC_{low} also increased with increasing temperature, but dropped to a value lower than baseline when temperature went back to body temperature. Moreover, the difference between ADC_{low} and ADC_{high} which is related to perfusion started to decrease when the heating region reach 48℃.

5.4 DISCUSSION

The f we discussed in this chapter is without T_2 correction. This is simply because that all the equation derivations started with the IVIM model without T_2 correction.

The conflict of the ADC_{high} variation with temperature between prostate and muscle tissue may be introduced by the blood perfusion amount. We know that the muscle is low perfusion tissue with f about 15%. This means the decrease of f when the microstructure started to change may be compensated by the increased of the diffusion-related term (the first term in Equation 5.1.3). This is how we got Equation 5.1.10. We assumed that the decrease of f was compensated by the increasing D_0, and this D_0 became a function of temperature (Equation 5.1.10). When the tissue went back to the body temperature, D_0 reached the maximum value (D_{0max}) and did not change in a short period of time.

However, the perfusion term containing *f* makes much more of a contribution in ADC_{low} because of the small *b* value. This is the reason why after heating, ADC_{low} did not go back to the baseline value when temperature of heated region went back to body temperature. The decreased *f* term is much larger than the increased D_{0max} term. We assume *f* decreased to a very small value, but still above zero, so the small *b* value introduced the difference between ADC_{low} and ADC_{high} after heating.

The decreasing starting point of perfusion term (the difference between ADC_{low} and ADC_{high} is *f* related) at 48℃ showed that the tissue microstructure may start to change at this temperature. Zhang reported that the tissue perfusion of muscle started to increase at 46℃[96]. These two temperatures are very close. And, according to the reported results and the results we got in our experiment, the perfusion-related term *D** maybe increase very fast around 48℃.

5.5 CONCLUSION

The change of tissue microstructures during heating includes three steps. The first step starts from the beginning of heating until the heated tissue reaching 48℃. D_0 and *f* do not change and the $ADC_{low/high}$ variation with temperature is only introduced by the increasing of *D* with temperature. The second step starts with heated tissue to 48℃, and continuous until the end of heating. During this period, D_0 increases with temperature and *f* decreases with temperature. At the end of heating, D_0 increases to the maximum value D_{0max}, which would not change during a short amount of time, and *f* decreases to very small value which approaches zero. The third step is the cooling period. *D* is the only reason causing $ADC_{low/high}$ varies with temperature.

In the low *f* tissue, such as muscle, the decreasing of *f* is compensated by the increasing of D_0 after heating, so ADC_{high} cannot be applied as a biomarker to test the tissue oblation in such kind of tissue. However, because *f* always contributes big part in ADC_{low} because of small *b* value, ADC_{low} can be applied as a thermal oblation biomarker even for low *f* tissue.

6 CONCLUSION, LIMITATIONS, AND FUTURE WORK

6.1 ACHIEVED SPECIFIC AIMS

Develop a modified T_2-weighted image sequence to decrease the scan time.

A modified multi-shot TSE sequence with variable refocusing angle was introduced in Chapter 4. The ZOOM technique was also applied to the modified sequence. The scan time was reduced to half of the previous scan time and the CNR between myometrium and fibroid increased from 7% to 9.4%.

Hypothesis 1 is proved.

Investigate the tissue microstructure and microcirculation for different types of fibroids classified by Funaki classification. Find out the difference between Type III fibroids and other treatable fibroids. Find out the reason why no significant perfusion difference for Type III fibroids reported in previous studies.

The simulation results reported in Chapter 3 show that T_2 decay had a large effect on the IVIM model. The reported results in previous works, which showed no significant difference of *f* value (f_c) for different types of fibroids, was because the T_2 decay effect was not taken into consideration. T_2 decay affected Type I fibroids much more than Type III fibroids.

The clinical results reported in Chapter 3 show that Type II fibroids had significant higher *f* value than Type I fibroids after T_2 correction. But without T_2 correction, the difference between these two types of fibroids is not statistic significant.

Hypothesis 2 is proved.

Clinical results also showed T_2 highly correlated to both *D* and f_c value. Both *D* and f_c exponentially increased with the increase of T_2 value. *D* also asymptotic increased relative to *D* of blood.

Develop a new NPV estimation tool which satisfies: (1) non-contrast involved and (2) high SNR and CNR.

DWI with low *b* value (20 s/mm^2) had higher SNR in the treated regions and higher CNR between treated and non-treated region compared to DWI obtained with high *b* value (1000 s/mm^2).

Thus, f_c map can be used as a non-contrast-involved method to estimate the NPV.

Hypothesis 3 is proved.

Investigate the tissue microstructure response to heat during sonication by studying the IVIM model.

During the heating, tissue microstructure starts to change at 48℃. Both *f* and D_0 change with temperature after tissue microstructure changed. At the end of heating, *f* approaches a very small value, and D_0 increases to a bigger value and would not change during a short among of time. ADC_{high} can be only applied as a bio-marker to detect tissue damage for tissues with high *f*.

Hypothesis 4 is proved.

6.2 LIMITATIONS AND FUTURE WORK

6.2.1 Limitations

The main limitation of the work reported in the dissertation is that no Type III fibroids clinical data were involved.

For the third specific aim, we only demonstrate that Type II fibroids had high f_c values than Type I fibroids, but no Type III clinical data were collected to support the hypothesis that Type III fibroids should have the highest f_c among all three types of fibroids.

6.2.2 Future work

(1) More clinical data will be collected in the future, especially data for Type III fibroids. The f_c of Type III fibroids will be calculated and to compare with the other two types of fibroids.

(2) IVIM tests will be applied to tissues with a range of diffusion and perfusion values, such as liver, spleen, and brain. The relationship between T_2 and D, T_2 and f_c will be investigated to find out whether the phenomena that D and f_c exponentially increased with increase of T_2 is tissue independent, and whether D asymptotic increases to the value of D of blood.

(3) Perfusion variations during heating measurement will be applied to MRgHIFU therapy of uterine fibroids or other tissues with high f value. f variation or ADC_{low} variation will be measured during heating to investigate how perfusion changes due to changes in temperature.

REFERENCE

1. Baird, Donna Day, David B. Dunson, Michael C. Hill, Deborah Cousins, and Joel M. Schectman. "High cumulative incidence of uterine leiomyoma in black and white women: ultrasound evidence." *American Journal of Obstetrics and Gynecology* 188, no. 1 (2003): 100-107.

2. Stewart EA. What is Uterine Fibroids. Stewart EA. Uterine Fibroids: The complete guide, 1st edition. Johns Hopkins University Press 2007: p3-7.

3. Farquhar, Cynthia M., and Claudia A. Steiner. "Hysterectomy rates in the United States 1990–1997." *Obstetrics & Gynecology* 99, no. 2 (2002): 229-234.

4. Stewart EA. What is Uterine Fibroids. Stewart EA. Uterine Fibroids: The complete guide, 1st edition. Johns Hopkins University Press 2007: p8-9.

5. Baird, Donna Day, David B. Dunson, Michael C. Hill, Deborah Cousins, and Joel M. Schectman. "High cumulative incidence of uterine leiomyoma in black and white women: ultrasound evidence." *American Journal of Obstetrics and Gynecology* 188, no. 1 (2003): 100-107.

6. Fedele, Luigi, Stefano Bianchi, Milena Dorta, Diana Brioschi, Fabrizio Zanotti, and Paolo Vercellini. "Transvaginal ultrasonography versus hysteroscopy in the diagnosis of uterine submucous myomas." *Obstetrics & Gynecology* 77, no. 5 (1991): 745-748.

7. Dueholm, Margit, Erik Lundorf, Estrid S. Hansen, Susanne Ledertoug, and Frede Olesen. "Accuracy of magnetic resonance imaging and transvaginal ultrasonography in the diagnosis, mapping, and measurement of uterine myomas." *American Journal of Obstetrics and Gynecology* 186, no. 3 (2002): 409-415.

8. Casillas, Javier, Ronald C. Joseph, and Jorge J. Guerra Jr. "CT appearance of uterine leiomyomas." *Radiographics* 10, no. 6 (1990): 999-1007.

9. Urban, B. A., and E. K. Fishman. "Spiral CT of the female pelvis: clinical applications." *Abdominal Imaging* 20, no. 1 (1995): 9-14.

10. Varras, M., S. Antoniou, Ch Samara, S. Frakala, Z. Angelidou-Manika, and P. Paissios. "Intraperitoneal haemorrhage secondary to perforation of uterine fibroid after cystic degeneration. Unusual CT findings resembling malignant pelvic tumor: case report." *European Journal of Gynaecological Oncology* 23, no. 6 (2001): 565-568.

11. Birchard, Katherine R., Michele A. Brown, W. Brian Hyslop, Zeynep Firat, and Richard C. Semelka. "MRI of acute abdominal and pelvic pain in pregnant patients." *American journal of Roentgenology* 184, no. 2 (2005): 452-458.

12. Spielmann, Audrey L., Ciaran Keogh, Bruce B. Forster, Michael L. Martin, and Lindsay S. Machan. "Comparison of MRI and sonography in the preliminary evaluation for fibroid embolization." *American Journal of Roentgenology* 187, no. 6 (2006): 1499-1504.

13. Hindley, Jonathan, Wladyslaw M. Gedroyc, Lesley Regan, Elizabeth Stewart, Clare Tempany, Kullervo Hynnen, Nathan Macdanold et al. "MRI guidance of focused ultrasound therapy of uterine fibroids: early results." *American Journal of Roentgenology* 183, no. 6 (2004): 1713-1719.

14. Funaki, Kaoru, Hidenobu Fukunishi, Tsuyoshi Funaki, Katsuhiro Sawada, Yasushi Kaji, and Takeshi Maruo. "Magnetic resonance-guided focused ultrasound surgery for uterine fibroids: relationship between the therapeutic effects and signal intensity of preexisting T2-weighted magnetic resonance images." *American Journal of Obstetrics and Gynecology* 196, no. 2 (2007): 184-e1.

15. Chan, Arthur H., Victor Y. Fujimoto, Donald E. Moore, Roy W. Martin, and Shahram Vaezy. "An image-guided high intensity focused ultrasound device for uterine fibroids treatment." *Medical Physics* 29, no. 11 (2002): 2611-2620.

16. Morita, Yutaka, Naoki Ito, Hiromi Hikida, Sawako Takeuchi, Kouji Nakamura, and Hirofumi Ohashi. "Non-invasive magnetic resonance imaging-guided focused ultrasound treatment for uterine fibroids–early experience." *European Journal of Obstetrics & Gynecology and Reproductive Biology* 139, no. 2 (2008): 199-203.

17. Hesley, Gina K., Krzysztof R. Gorny, Tara L. Henrichsen, David A. Woodrum, and Douglas L. Brown. "A clinical review of focused ultrasound ablation with magnetic resonance guidance: an option for treating uterine fibroids." *Ultrasound Quarterly* 24, no. 2 (2008): 131-139.

18. Hesley, Gina K., Joel P. Felmlee, John B. Gebhart, Kelly T. Dunagan, Krzysztof R. Gorny, Jessica B. Kesler, Kathleen R. Brandt, Janel N. Glantz, and Bobbie S. Gostout. "Noninvasive treatment of uterine fibroids: early Mayo Clinic experience with magnetic resonance imaging-guided focused ultrasound." In *Mayo Clinic Proceedings*, vol. 81, no. 7: 936-942. Elsevier, 2006.

19. Voogt, M. J., H. Trillaud, Y. S. Kim, WP Th M. Mali, J. Barkhausen, L. W. Bartels, R. Deckers et al. "Volumetric feedback ablation of uterine fibroids using magnetic resonance-guided high intensity focused ultrasound therapy." *European Radiology* 22, no. 2 (2012): 411-417.

20. Mikami, Koji, Takamichi Murakami, Atsuya Okada, Keigo Osuga, Kaname Tomoda, and Hironobu Nakamura. "Magnetic resonance imaging-guided focused ultrasound ablation of uterine fibroids: early clinical experience." *Radiation Medicine* 26, no. 4 (2008): 198-205.

21. Fennessy, Fiona M., and Clare M. Tempany. "A review of magnetic resonance imaging-guided focused ultrasound surgery of uterine fibroids." *Topics in Magnetic Resonance Imaging* 17, no. 3 (2006): 173-179.

22. Fennessy, Fiona M., and Clare M. Tempany. "MRI-guided focused ultrasound surgery of uterine leiomyomas 1." *Academic Radiology* 12, no. 9 (2005): 1158-1166.

23. Stewart, Elizabeth A., Wladyslaw MW Gedroyc, Clare MC Tempany, Bradley J. Quade, Yael Inbar, Tilman Ehrenstein, Asher Shushan et al. "Focused ultrasound treatment of uterine fibroid tumors: safety and feasibility of a noninvasive thermoablative technique." *American Journal of Obstetrics and Gynecology* 189, no. 1 (2003): 48-54.

24. Cura, M., A. Cura, and A. Bugnone. "Role of magnetic resonance imaging in patient selection for uterine artery embolization." *Acta Radiologica* 47, no. 10 (2006): 1105-1114.

25. Mara, Michal, Jana Maskova, Zuzana Fucikova, David Kuzel, Tomas Belsan, and Ondrej Sosna. "Midterm clinical and first reproductive results of a randomized controlled trial comparing uterine fibroid embolization and myomectomy." *Cardiovascular and Interventional Radiology* 31, no. 1 (2008): 73-85.

26. Freed, Max M., and James B. Spies. "Uterine artery embolization for fibroids: a review of current outcomes." *Seminars in Reproductive Medicine*, vol. 28, no. 3(2010): 235-241.

27. Andersen, P. E., N. Lund, P. Justesen, T. Munk, B. Elle, and C. Floridon. "Uterine artery embolization of symptomatic uterine fibroids." *Acta Radiologica* 42, no. 2 (2001): 234-238.

28. Volkers, Nicole A., Wouter JK Hehenkamp, Erwin Birnie, Willem M. Ankum, and Jim A. Reekers. "Uterine artery embolization versus hysterectomy in the treatment of symptomatic uterine fibroids: 2 years' outcome from the randomized EMMY trial." *American Journal of Obstetrics and Gynecology* 196, no. 6 (2007): 519-e1.

29. Samadi, Aziz R., Nancy C. Lee, W. Dana Flanders, J. R. Boring 3rd, and Ewart B. Parris. "Risk factors for self-reported uterine fibroids: a case-control study." *American Journal of Public Health* 86, no. 6 (1996): 858-862.

30. Stewart EA. What is Uterine Fibroids. Stewart EA. Uterine Fibroids: The complete guide, 1st edition. Johns Hopkins University Press 2007: p16-17.

31. Cura, M., A. Cura, and A. Bugnone. "Role of magnetic resonance imaging in patient selection for uterine artery embolization." *Acta Radiologica* 47, no. 10 (2006): 1105-1114.

32. Mara, Michal, Jana Maskova, Zuzana Fucikova, David Kuzel, Tomas Belsan, and Ondrej Sosna. "Midterm clinical and first reproductive results of a randomized controlled trial comparing uterine fibroid embolization and myomectomy." *Cardiovascular and Interventional Radiology* 31, no. 1 (2008): 73-85.

33. Lepine, Lisa A., S. D. Hillis, P. A. Marchbanks, L. M. Koonin, B. Morrow, B. A. Kieke, and L. S. Wilcox. "Hysterectomy surveillance--United States, 1980-1993." *MMWR. CDC surveillance summaries: Morbidity and mortality weekly report. CDC Surveillance Summaries/Centers for Disease Control* 46, no. 4 (1997): 1-15.

34. Vessey, Martin P., L. A. U. R. E. N. C. E. Villard-Mackintosh, Klim Mcpherson, Angela Coulter, and David Yeates. "The epidemiology of hysterectomy: findings in a large cohort study." *BJOG: An International Journal of Obstetrics & Gynaecology* 99, no. 5 (1992): 402-407.

35. Guarnaccia, Michael M., and Mitchell S. Rein. "Traditional surgical approaches to uterine fibroids: abdominal myomectomy and hysterectomy." *Clinical Obstetrics and Gynecology* 44, no. 2 (2001): 385-400.

36. Hutchins Jr, Francis L. "Abdominal myomectomy as a treatment for symptomatic uterine fibroids." *Obstetrics and Gynecology Clinics of North America* 22, no. 4 (1995): 781-789.

37. Dessolle, Lionel, David Soriano, Christophe Poncelet, Jean-Louis Benifla, Patrick Madelenat, and Emile Daraï. "Determinants of pregnancy rate and obstetric outcome after laparoscopic myomectomy for infertility." *Fertility and Sterility* 76, no. 2 (2001): 370-374.

38. Li, T. C., R. Mortimer, and I. D. Cooke. "Myomectomy: a retrospective study to examine reproductive performance before and after surgery." *Human Reproduction* 14, no. 7 (1999): 1735-1740.

39. http://coe.ucsf.edu/coe/fibroid/treatments.html

40. Practice Committee of the American Society for Reproductive Medicine in collaboration with the Society of Reproductive Surgeons. "Myomas and reproductive function." *Fertility and Sterility* 90.5 (2008): S125-S130.

41. Zhao, Wen-Peng, Jin-Yun Chen, Lian Zhang, Quan Li, Juan Qin, Song Peng, Ke-Quan Li, Zhi-Biao Wang, and Wen-Zhi Chen. "Feasibility of ultrasound-guided high intensity focused ultrasound ablating uterine fibroids with hyperintense on T2-weighted MR imaging." *European Journal of Radiology* 82, no. 1 (2013): e43-e49.

42. Kim, Young-sun, Hyo K. Lim, Jae-Hun Kim, Hyunchul Rhim, Byung Kwan Park, Bilgin Keserci, Max O. Köhler et al. "Dynamic contrast-enhanced magnetic

resonance imaging predicts immediate therapeutic response of magnetic resonance-guided high-intensity focused ultrasound ablation of symptomatic uterine fibroids." *Investigative Radiology* 46, no. 10 (2011): 639-647.

43. Rouvière, Olivier, Denis Lyonnet, Anne Raudrant, Catherine Colin-Pangaud, Jean Yves Chapelon, Raymonde Bouvier, Jean Michel Dubernard, and Albert Gelet. "MRI appearance of prostate following transrectal HIFU ablation of localized cancer." *European Urology* 40, no. 3 (2001): 265-274.

44. Kim, Chan Kyo, Byung Kwan Park, Hyun Moo Lee, Sam Soo Kim, and EunJu Kim. "MRI techniques for prediction of local tumor progression after high-intensity focused ultrasonic ablation of prostate cancer." *American Journal of Roentgenology* 190, no. 5 (2008): 1180-1186.

45. Illing, R. O., J. E. Kennedy, F. Wu, G. R. Ter Haar, A. S. Protheroe, P. J. Friend, F. V. Gleeson, D. W. Cranston, R. R. Phillips, and M. R. Middleton. "The safety and feasibility of extracorporeal high-intensity focused ultrasound (HIFU) for the treatment of liver and kidney tumours in a Western population." *British Journal of Cancer* 93, no. 8 (2005): 890-895.

46. Quesson, Bruno, Mathilde Merle, Max O. Köhler, Charles Mougenot, Sebastien Roujol, Baudouin Denis De Senneville, and Chrit T. Moonen. "A method for MRI guidance of intercostal high intensity focused ultrasound ablation in the liver." *Medical Physics* 37, no. 6 (2010): 2533-2540.

47. Brown, Mark A., and Richard C. Semelka. *MRI: Basic Principles and Applications*. John Wiley & Sons, 2011.

48. Hashemi, Ray Hashman, William G. Bradley, and Christopher J. Lisanti. *MRI: the basics*. Lippincott Williams & Wilkins, 2012.

49. Bushong, Stewart C., and Geoffrey Clarke. *Magnetic resonance Imaging: Physical and Biological Principles*. Elsevier Health Sciences, 2013.

50. Muthupillai, R., D. J. Lomas, P. J. Rossman, J. F. Greenleaf, A. Manduca, and R. L. Ehman. "Magnetic resonance elastography by direct visualization of propagating acoustic strain waves." *Science* 269, no. 5232 (1995): 1854-1857.
51. Yin, Meng, Jayant A. Talwalkar, Kevin J. Glaser, Armando Manduca, Roger C. Grimm, Phillip J. Rossman, Jeff L. Fidler, and Richard L. Ehman. "Assessment of hepatic fibrosis with magnetic resonance elastography." *Clinical Gastroenterology and Hepatology* 5, no. 10 (2007): 1207-1213.

52. Huwart, Laurent, Christine Sempoux, Eric Vicaut, Najat Salameh, Laurence Annet, Etienne Danse, Frank Peeters et al. "Magnetic resonance elastography for the noninvasive staging of liver fibrosis." *Gastroenterology* 135, no. 1 (2008): 32-40.

53. Moros, Eduardo, ed. *Physics of Thermal Therapy: Fundamentals and Clinical Applications*. CRC Press, 2012.

54. Köhler, Max O., Charles Mougenot, Bruno Quesson, Julia Enholm, Brigitte Le Bail, Christophe Laurent, Chrit TW Moonen, and Gösta J. Ehnholm. "Volumetric HIFU ablation under 3D guidance of rapid MRI thermometry." *Medical physics* 36, no. 8 (2009): 3521-3535.

55. McGibney, G., M. R. Smith, S. T. Nichols, and A. Crawley. "Quantitative evaluation of several partial Fourier reconstruction algorithms used in MRI." *Magnetic resonance in medicine* 30, no. 1 (1993): 51-59.

56. Margosian, Paul M., Gordon DeMeester, and Haiying Liu. "Partial Fourier acquisition in MRI." *eMagRes* (2007).

57. Gousse, Angelo E., Zoran L. Barbaric, Michael H. Safir, Shahar Madjar, Alan K. Marumoto, and Shlomo Raz. "Dynamic half Fourier acquisition, single shot turbo spin-echo magnetic resonance imaging for evaluating the female pelvis." *The Journal of Urology* 164, no. 5 (2000): 1606-1613.

58. Yu, Jeong-Sik, Ki Whang Kim, Young Hwan Kim, Eun-Kee Jeong, and Daisy Chien. "Comparison of multishot turbo spin echo and HASTE sequences for T2-weighted MRI of liver lesions." *Journal of Magnetic Resonance Imaging* 8, no. 5 (1998): 1079-1084.

59. Pruessmann, Klaas P., Markus Weiger, Markus B. Scheidegger, and Peter Boesiger. "SENSE: sensitivity encoding for fast MRI." *Magnetic Resonance in Medicine* 42, no. 5 (1999): 952-962.

60. Weiger, Markus, Klaas P. Pruessmann, and Peter Boesiger. "2D SENSE for faster 3D MRI." *Magnetic Resonance Materials in Physics, Biology and Medicine* 14, no. 1 (2002): 10-19.

61. Liu, Jing, Bilgin Keserci, Xuedong Yang, Juan Wei, Rong Rong, Ying Zhu, and Xiaoying Wang. "Volume transfer constant (K trans) maps from dynamic contrast enhanced MRI as potential guidance for MR-guided high intensity focused ultrasound treatment of hypervascular uterine fibroids." *Magnetic Resonance Imaging* 32, no. 9 (2014): 1156-1161.

62. Marianne J., Marijn van Stralen, Marlijne E. Ikink, Roel Deckers, Koen L. Vincken, Lambertus W. Bartels, P. Th M. Willem, and Maurice AAJ van den Bosch. "Targeted vessel ablation for more efficient magnetic resonance-guided high-intensity focused ultrasound ablation of uterine fibroids." *Cardiovascular and Interventional Radiology* 35, no. 5 (2012): 1205-1210.

63. Kim, Young-sun, Jae-Hun Kim, Hyunchul Rhim, Hyo Keun Lim, Bilgin Keserci, Duk-Soo Bae, Byoung-Gie Kim, Jeong-Won Lee, Tae-Joong Kim, and Chel Hun

Choi. "Volumetric MR-guided high-intensity focused ultrasound ablation with a one-layer strategy to treat large uterine fibroids: initial clinical outcomes." *Radiology* 263, no. 2 (2012): 600-609.

64. Zsuzanna M. Lenard, Natha J. McDannold, Fiona M. Fennessy, Elizabeth A. Stewart, Ferenc A. Jolesz, Kullervo Hynynen, Clare M, C. Tempany, Uterine leiomyomas: mr imging-guided focused ultrasound surgery—imaging predictor of success, *Radiology* 249,no.1, (2008): 187-194.

65. Zhao, Wen-Peng, Jin-Yun Chen, and Wen-Zhi Chen. "Effect of biological characteristics of different types of uterine fibroids, as assessed with T2-weighted magnetic resonance imaging, on ultrasound-guided high-intensity focused ultrasound ablation." *Ultrasound in Medicine & Biology* 41, no. 2 (2015): 423-431.

66. Wang R, Fu H, Zhang H, Li CX, Yang J. The comparison of diffusion and perfusion characteristics among the different types of uterine fibroids based on T2WIs: and intravoxel incoherent motion MRI study. Proceedings of the 22th Annual Meeting of ISMRM, Milan, 2014(abstract 2598).

67. Ikink ME, van Breugel JMM, Nijenhuis RJ et al. Intra voxel inchoherent motion MRI for the characterization of uterine fibroids before MR-guided high-intensity focused ultrasound ablation. Proceedings of the 22th Annual Meeting of ISMRM, Milan, 2014(abstract 3693).

68. Jacobs, Michael A., Ronald Ouwerkerk, Ihab Kamel, Paul A. Bottomley, David A. Bluemke, and Hyun S. Kim. "Proton, diffusion-weighted imaging, and sodium (23Na) MRI of uterine leiomyomata after MR-guided high-intensity focused ultrasound: A preliminary study." *Journal of Magnetic Resonance Imaging* 29, no. 3 (2009): 649-656.

69. Ikink, Marlijne E., Marianne J. Voogt, Maurice AAJ van den Bosch, Robbert J. Nijenhuis, Bilgin Keserci, Young-sun Kim, Koen L. Vincken, and Lambertus W. Bartels. "Diffusion-weighted magnetic resonance imaging using different b-value combinations for the evaluation of treatment results after volumetric MR-guided high-intensity focused ultrasound ablation of uterine fibroids." *European Radiology* 24, no. 9 (2014): 2118-2127.

70. Jacobs, Michael A., Edward H. Herskovits, and Hyun S. Kim. "Uterine Fibroids: Diffusion-weighted MR Imaging for Monitoring Therapy with Focused Ultrasound Surgery—Preliminary Study 1." *Radiology* 236, no. 1 (2005): 196-203.

71. Pilatou, Magdalini C., Elizabeth A. Stewart, Stephan E. Maier, Fiona M. Fennessy, Kullervo Hynynen, Clare Tempany, and Nathan McDannold. "MRI-based thermal dosimetry and diffusion-weighted imaging of MRI-guided focused ultrasound thermal ablation of uterine fibroids." *Journal of Magnetic Resonance Imaging* 29, no. 2 (2009): 404-411.

72. Qu FF, Pednekar A, Hor PH, et al. Non-Contrast Assessment Microvascular Blood Flow Fraction to Evaluate Treatment Efficiency of MR guided High-Intensity Focused Ultrasound (MR-HIFU) Surgery of Uterine Fibroids. In: Proceedings of the 22th Annual Meeting of ISMRM, Milan, 2014(abstract 3679).

73. Le Bihan, Denis, Eric Breton, Denis Lallemand, M. L. Aubin, J. Vignaud, and M. Laval-Jeantet. "Separation of diffusion and perfusion in intravoxel incoherent motion MR imaging." *Radiology* 168, no. 2 (1988): 497-505.

74. Penner, A-H., A. M. Sprinkart, G. M. Kukuk, I. Gütgemann, J. Gieseke, H. H. Schild, W. A. Willinek, and P. Mürtz. "Intravoxel incoherent motion model-based liver lesion characterisation from three b-value diffusion-weighted MRI." *European Radiology* 23, no. 10 (2013): 2773-2783.

75. Luciani, Alain, Alexandre Vignaud, Madeleine Cavet, Jeanne Tran Van Nhieu, Ariane Mallat, Lucile Ruel, Alexis Laurent, Jean-François Deux, Pierre Brugieres, and Alain Rahmouni. "Liver cirrhosis: intravoxel incoherent motion MR imaging—Pilot study 1." *Radiology* 249, no. 3 (2008): 891-899.

76. Sigmund, E. E., G. Y. Cho, S. Kim, M. Finn, M. Moccaldi, J. H. Jensen, D. K. Sodickson, J. D. Goldberg, S. Formenti, and L. Moy. "Intravoxel incoherent motion imaging of tumor microenvironment in locally advanced breast cancer." *Magnetic Resonance in Medicine* 65, no. 5 (2011): 1437-1447.

77. Liu, Chunling, Changhong Liang, Zaiyi Liu, Shuixing Zhang, and Biao Huang. "Intravoxel incoherent motion (IVIM) in evaluation of breast lesions: comparison with conventional DWI." *European Journal of Radiology* 82, no. 12 (2013): e782-e789.

78. Döpfert, Jörg, Andreas Lemke, Anja Weidner, and Lothar R. Schad. "Investigation of prostate cancer using diffusion-weighted intravoxel incoherent motion imaging." *Magnetic Resonance Imaging* 29, no. 8 (2011): 1053-1058.

79. Pang, Yuxi, Baris Turkbey, Marcelino Bernardo, Jochen Kruecker, Samuel Kadoury, Maria J. Merino, Bradford J. Wood, Peter A. Pinto, and Peter L. Choyke. "Intravoxel incoherent motion MR imaging for prostate cancer: an evaluation of perfusion fraction and diffusion coefficient derived from different b-value combinations." *Magnetic Resonance in Medicine* 69, no. 2 (2013): 553-562.

80. Pekar, James, Chrit TW Moonen, and Peter van Zijl. "On the precision of diffusion/perfusion imaging by gradient sensitization." *Magnetic Resonance in Medicine* 23, no. 1 (1992): 122-129.

81. Woodhams, Reiko, Keiji Matsunaga, Shinichi Kan, Hirofumi Hata, Masanori Ozaki, Keiichi Iwabuchi, Masaru Kuranami, Masahiko Watanabe, and Kazushige Hayakawa. "ADC mapping of benign and malignant breast tumors." *Magnetic Resonance in Medical Sciences* 4, no. 1 (2005): 35-42.

82. Guo, Yong, You-Quan Cai, Zu-Long Cai, Yuan-Gui Gao, Ning-Yu An, Lin Ma, Srikanth Mahankali, and Jia-Hong Gao. "Differentiation of clinically benign and malignant breast lesions using diffusion-weighted imaging." *Journal of Magnetic Resonance Imaging* 16, no. 2 (2002): 172-178.

83. Lemke, Andreas, Frederik B. Laun, Dirk Simon, Bram Stieltjes, and Lothar R. Schad. "An in vivo verification of the intravoxel incoherent motion effect in diffusion-weighted imaging of the abdomen." *Magnetic Resonance in Medicine* 64, no. 6 (2010): 1580-1585.

84. Lee S, Lee JM, Yoon JH, Kabasawa H. IVIM with simultaneous T2 mapping and relaxivity correction. Proceedings of the 21th Annual Meeting of ISMRM, Salt Lake City, 2013(abstract 3109).

85. Stanisz, Greg J., Ewa E. Odrobina, Joseph Pun, Michael Escaravage, Simon J. Graham, Michael J. Bronskill, and R. Mark Henkelman. "T1, T2 relaxation and magnetization transfer in tissue at 3T." *Magnetic Resonance in Medicine* 54, no. 3 (2005): 507-512.

86. Bihan, Denis Le, and Robert Turner. "The capillary network: a link between IVIM and classical perfusion." *Magnetic Resonance in Medicine* 27, no. 1 (1992): 171-178.

87. Buecker, Arno, Gerhard Adam, Joerg M. Neuerburg, Arndt Glowinski, Joop J. van Vaals, and Rolf W. Guenther. "MR-guided biopsy using a T2-weighted single-shot Zoom Imaging sequence (Local Look technique)." *Journal of Magnetic Resonance Imaging* 8, no. 4 (1998): 955-959.

88. Hennig, Jürgen. "Echoes—how to generate, recognize, use or avoid them in MR-imaging sequences. Part I: Fundamental and not so fundamental properties of spin echoes." *Concepts in Magnetic Resonance* 3, no. 3 (1991): 125-143.

89. Hennig, Juergen, Matthias Weigel, and Klaus Scheffler. "Calculation of flip angles for echo trains with predefined amplitudes with the extended phase graph (EPG)-algorithm: Principles and applications to hyperecho and TRAPS sequences." *Magnetic Resonance in Medicine* 51, no. 1 (2004): 68-80.

90. Alsop, David C. "The sensitivity of low flip angle RARE imaging." *Magnetic Resonance in Medicine* 37, no. 2 (1997): 176-184.

91. Busse, Reed F., Hari Hariharan, Anthony Vu, and Jean H. Brittain. "Fast spin echo sequences with very long echo trains: design of variable refocusing flip angle schedules and generation of clinical T2 contrast." *Magnetic Resonance in Medicine* 55, no. 5 (2006): 1030-1037.

92. Madhuranthakam, A. J., R. F. Busse, J. H. Brittain, N. M. Rofsky, and D. C. Alsop. "Sensitivity of low flip angle SSFSE of the abdomen to cardiac motion." *Proceedings of the ISMRM, Berlin* (2007): 2523.

93. Juan C. Plata, Andrew B. Holbrook, Michael Marx, and Vasant Salgaonkar et al. Apparent Diffusion Coefficient Decrease During Thermal Ablation of the Prostate as an Early Indicator for Loss of Tissue Viability. Proceedings of the 21th Annual Meeting of ISMRM, Salt Lake City, 2013(abstract 0227).

94. Madhuranthakam, A. J., R. F. Busse, J. H. Brittain, N. M. Rofsky, and D. C. Alsop. "Sensitivity of low flip angle SSFSE of the abdomen to cardiac motion." *Proceedings of the ISMRM, Berlin* (2007): 2523.

95. Chang, D. C., H. E. Rorschach, B. L. Nichols, and C. F. Hazlewood. "Implications of diffusion coefficient measurements for the structure of cellular water*." *Annals of the New York Academy of Sciences* 204, no. 1 (1973): 434-443.

96. Zhang, J., P. H. Hor, J. Fischer, A. Partanen, T. Karjalainen, and R. Muthupillai. "A temperature dependent perfusion rate model for simulating temperature evolution in tissue for magnetic resonance imaging guided high intensity focused ultrasound (MR-HIFU) therapy: initial experience in a pig model." In *Proc. Intl. Soc. Magnetic Resonance in Medicine*, vol. 19, p. 3716. 2011.